

WIYN OPEN CLUSTER STUDY.LXXVI. LI EVOLUTION AMONG STARS OF LOW/INTERMEDIATE MASS:
THE METAL-DEFICIENT OPEN CLUSTER, NGC 2506

BARBARA J. ANTHONY-TWAROG

Department of Physics and Astronomy, University of Kansas, Lawrence, KS 66045-7582, USA

DONALD B. LEE-BROWN

Department of Physics and Astronomy, University of Kansas, Lawrence, KS 66045-7582, USA

CONSTANTINE P. DELIYANNIS

Department of Astronomy, Indiana University, Bloomington, IN 47405-7105

BRUCE A. TWAROG

Department of Physics and Astronomy, University of Kansas, Lawrence, KS 66045-7582, USA

ABSTRACT

HYDRA spectra of 287 stars in the field of NGC 2506 from the turnoff through the giant branch are analyzed. With previous data, 22 are identified as probable binaries; 90 more are classified as potential non-members. Spectroscopic analyses of ~ 60 red giants and slowly rotating turnoff stars using line equivalent widths and a neural network approach lead to $[\text{Fe}/\text{H}] = -0.27 \pm 0.07$ (s.d.) and $[\text{Fe}/\text{H}] = -0.27 \pm 0.06$ (s.d.), respectively. Li abundances are derived for 145 probable single-star members, 44 being upper limits. Among turnoff stars outside the Li-dip, $A(\text{Li}) = 3.04 \pm 0.16$ (s.d.), with no trend with color, luminosity, or rotation speed. Evolving from the turnoff across the subgiant branch, there is a well-delineated decline to $A(\text{Li}) \sim 1.25$ at the giant branch base, coupled with the rotational spindown from between ~ 20 and 70 km s^{-1} to less than 20 km s^{-1} for stars entering the subgiant branch and beyond. $A(\text{Li})$ remains effectively constant from the giant branch base to the red giant clump level. A new member above the clump redefines the path of the first-ascent red giant branch; its Li is 0.6 dex below the first-ascent red giants. With one exception, all post-He-flash stars have upper limits to $A(\text{Li})$, at or below the level of the brightest first-ascent red giant. The patterns are in excellent qualitative agreement with the model predictions for low/intermediate-mass stars which undergo rotation-induced mixing at the turnoff and subgiant branch, first dredge-up, and thermohaline mixing beyond the red giant bump.

Keywords: open clusters and associations: individual (NGC 2506) - stars: abundances

1. INTRODUCTION

This paper presents a spectroscopic complement to the intermediate-band photometric analysis of the old open cluster, NGC 2506 (Anthony-Twarog et al. (2016), hereinafter AT16). The background history of this clus-

ter is explored in detail in AT16 and will not be repeated here except when required by the specifics of the analysis. Suffice it to say that precision photometry on the extended Strömgen system ($uvbyCaH\beta$) has established that the cluster is subject to low reddening ($E(B-V) = 0.058 \pm 0.001$) with negligible variation across its face (AT16). More important for our purposes, as derived from two photometric indices, the cluster is moderately metal-poor ($[\text{Fe}/\text{H}] = -0.32 \pm 0.03$) relative to the typical cluster in the solar neighborhood, a not unexpected result for a cluster positioned beyond

bjat@ku.edu

donald@ku.edu

cdehlyan@indiana.edu

btwarog@ku.edu

the solar circle in the anticenter region (e.g., [Twarog, Ashman, & Anthony-Twarog 1997](#); [Friel et al. 2002](#); [Netopil et al. 2016](#)). The key element, however, enhancing its role is its age, now well established at 1.85 ± 0.05 Gyr based upon application of the Victoria-Regina (VR) isochrones ([VandenBerg, Bergbusch, & Dowler 2006](#)) on the Strömgen system. The revised cluster age places NGC 2506 in a category comparable to NGC 3680 at 1.7 Gyr ([Anthony-Twarog et al. 2009](#)), but slightly older than NGC 752 at 1.45 Gyr ([Twarog et al. 2015](#)) and IC 4651 at 1.5 Gyr ([Anthony-Twarog et al. 2009](#)); these clusters cover a range in metallicity of ~ 0.45 dex in $[\text{Fe}/\text{H}]$.

Since the overarching goal of our cluster program is to evaluate and understand the role of mixing/convection in the atmospheres and interiors of stars of low to intermediate mass both on and off the main sequence, NGC 2506 holds a pivotal position between the younger clusters like NGC 7789 (1.4 Gyr) and NGC 752 and the clearly older example of NGC 6819 (2.25 Gyr) ([Lee-Brown et al. 2015](#); [Deliyannis et al. 2018](#)). The slightly lower turnoff mass of NGC 2506 due to the higher age and lower $[\text{Fe}/\text{H}]$, coupled with the richness of the cluster, allows delineation of the subgiant branch between the turnoff and the first-ascent red giant (FRG) branch below the red giant clump to a degree previously impossible, even with the combined samples of NGC 3680, NGC 752 and IC 4651 ([Anthony-Twarog et al. 2009](#)).

The outline of the paper is as follows: Sec. 2 discusses the compilation of potential spectroscopic candidates within NGC 2506, with special emphasis on the subgiant branch and stars fainter than the red giant clump, and the HYDRA observations that form the core of this study; Sec. 3 uses radial velocities and proper motions, when available, to identify and isolate the most probable members, whether single stars or binaries, and to eliminate likely field stars from the analysis. Sec. 4 lays out the metallicity derivation of the cluster for key elements adopting a traditional technique based upon the equivalent widths of lines in a modest wavelength region centered on the Li 6708 Å line, as well as a new approach for temperature and metallicity estimation built around a neural network. Sec. 5 contains the derivation of the Li abundance and demonstrates the critical place of NGC 2506 in probing the role of mixing/convection for stars evolving from the main sequence to the giant branch. Sec. 6 is a summary of our conclusions.

2. OBSERVATIONS AND DATA REDUCTION

2.1. Sample Selection

The starting point for the selection of potential cluster members is the proper-motion study of [Chiu & van Altena \(1981\)](#). There is little doubt that the stars defined

as 70% or higher probable members based upon proper motion alone form a well-defined sample which nicely delineates the primary cluster sequences in both broad-band ([McClure, Twarog, & Forrester 1981](#); [Marconi et al. 1997](#); [Kim et al. 2001](#)) and intermediate-band (AT16) photometry. The weaknesses in relying solely upon this selection criterion are apparent: (a) even with a rather high proper-motion probability cutoff of 70%, field star contamination can occur in the absence of the third vector component, the radial velocity; (b) proper-motion precision declines with increasing V , leading to the elimination of a higher fraction of true members and contamination by more non-members at the turnoff and fainter; and (c) the proper-motion and original broad-band surveys extend radially to only $\sim 5'$ from the cluster center. Though the dominant majority of the cluster members should be contained within this zone ([Lee, Kang, & Ann 2013](#)), the desire to populate and survey the color-magnitude diagram (CMD) as completely as possible, especially along some of the relatively rapid phases of evolution beyond the the main sequence, requires a broader search to identify as many NGC 2506 inhabitants as possible.

2.2. Photometric Input

To expand the sample, use was made of two CCD surveys covering comparable fields-of-view, i.e. $20'$ on a side. Three broad-band CCD surveys of NGC 2506 have been undertaken to date by [Marconi et al. \(1997\)](#); [Kim et al. \(2001\)](#); [Lee, Kang, & Ann \(2012\)](#); the surveys cover too small an area, suffer from larger than acceptable photometric scatter, or remain unpublished, respectively. The broad-band data for the current discussion ([Van Stockum et al. 2005](#)) were obtained on 6 November 2004 with the S2KB CCD at the f/7.5 focus of the WIYN 0.9m telescope at Kitt Peak National Observatory, with a scale of $0.60''$ per pixel, and seeing in the range $1.3'' - 1.6''$. Cluster images were reduced using DAOPHOT II ([Stetson 1986](#)). Typically, a few hundred bright, isolated stars were used to determine a point-spread-function, which was allowed to vary spatially, and a subsequent small (typically 0.01 - 0.02 mag) aperture correction, which was also allowed to vary spatially. After rejection of outliers, approximately 50 [Landolt \(1992\)](#) standards for each filter provided a calibration onto the Johnson-Cousins-Landolt system, and verified the photometricity of the night, as defined by zero-point errors in the transformations below 0.01 mag. The intermediate-band photometry (AT16) came from the 4000×4000 CCD camera¹ on the 1.0m telescope

¹ <http://www.astronomy.ohio-state.edu/Y4KCam/detector>

operated by the SMARTS² consortium at Cerro Tololo Inter-American Observatory. All stars with membership probabilities greater than 90% were used to define mean relations from the main sequence at V brighter than 15.6 to the top of the giant branch. Stars whose broadband photometric errors placed them within the range of the mean relations and had proper-motion probabilities above 50% were identified and initially selected. For stars outside the spatial range of the astrometric survey, location within range of the CMD relations provided the sole criterion for potential followup observations.

2.3. Spectroscopic Observations

Spectroscopic data were obtained using the WIYN 3.5m telescope³ and the HYDRA multi-object spectrograph over 19 nights from 16/17 January 2015 to 24/25 February, 2017. Nine configurations were designed to position fibers on a total of 287 stars, with 38 stars observed in more than one fiber configuration. Individual exposures ranged from 10 to 90 minutes, with accumulated totals of two hours for stars in the brightest two configurations targeting red giants, 5 to 7.5 hours for the four configurations aimed at subgiant stars, and between 9 and 12.5 hours total for three constructed to sample the turnoff region and upper main sequence of the cluster.

In these 58 hours of observing over a 25 month period, we obtained spectra with signal-to-noise per pixel ≥ 100 for all 287 stars. Our spectra cover a wavelength range ~ 400 Å wide centered on 6650 Å with per-pixel resolution of 0.2 Å and a resolution of $R \sim 13000$. Details on the reduction procedure can be found in Lee-Brown et al. (2015) and will not be repeated here.

Multiple exposures of any particular fiber configuration were combined if the observations were obtained within the same run of a few adjacent nights. A few of our configurations were observed over a period of a year or more, with some fiber losses in the interim. In these cases, the combination of individual spectra for stars obtained through different fibers or in different years was accomplished by undoing the individual throughput corrections before combining the spectra. This was also the procedure for stars observed in different runs as part of different fiber configurations. Combination of spectra from widely separated epochs was only carried out if there appeared to be no significant velocity shift.

As always, inclusion of specific stars within the spectroscopic survey was ultimately constrained by the need

to optimize HYDRA configurations over multiple observing runs. As preliminary reductions revealed that some stars were clear radial-velocity non-members, these were dropped from the program and others, usually potential subgiants and giants, were added. A small set of definite non-members was included in the data base to use as a control for comparison with the hopefully homogeneous group of metal-deficient cluster members.

Before discussing the results for individual stars, it should be noted that, whenever available, a star will be referred to using its WEBDA identification. However, since the sample here covers a much broader area than that of past published surveys, regrettably another identification number must be added for those stars outside the area listed within WEBDA. Column 1 of Table 1 lists WEBDA identification numbers for stars; numbers greater than 7000 refer to stars added by this survey. Table 1 lists stars in sequence based upon their right ascension; coordinates given in Table 1 are identical to those found in AT16 for all but 10 stars not included in the photometric study. The typeset version of Table 1 includes enough lines to show the form and content of the larger table available online.

A point of confusion regarding the WEBDA identifications does require correction. In the original photometric and astrometric surveys (McClure, Twarog, & Forrester 1981; Chiu & van Altena 1981), the stars were numbered using a quadrant number, ring number, and sequential count within that zone. For quadrant 2, ring 3, the number of stars extended to 106, so the last star measured was 23106. WEBDA incorrectly rewrote the numbers above 100 as ring 4, i.e. 23106 became 2406. This leads to confusion because in quadrants 2 and 4, there are photoelectric standards outside the three rings of the photographic survey numbered 2401, 2402, 4401, and 4402. WEBDA 2401 and 2402 are actually 23101 and 23102. In our Table and analysis, 2401 and 2402 refer to the original designations as marked on the cluster chart (Fig. 1) of McClure, Twarog, & Forrester (1981).

2.4. Radial Velocities and Rotation

Individual heliocentric stellar radial velocities, V_{rad} , were derived from each summed composite spectrum utilizing the Fourier-transform, cross-correlation facility *fxcor* in IRAF⁴. In this utility, program stars are compared to stellar templates of similar effective temperature (T_{eff}) over the full wavelength range of our spectra excluding the immediate vicinity of the $H\alpha$ line. Output of the *fxcor* utility characterizes the cross cor-

² <http://www.astro.yale.edu/smarts>

³ The WIYN Observatory was a joint facility of the University of Wisconsin-Madison, Indiana University, Yale University, and the National Optical Astronomy Observatory.

⁴ IRAF is distributed by the National Optical Astronomy Observatory, which is operated by the Association of Universities for Research in Astronomy, Inc., under cooperative agreement with the National Science Foundation.

Table 1. Velocity and Membership Information for Spectroscopic Sample in NGC 2506

ID No.	$\alpha(2000)$	$\delta(2000)$	Prob(μ)	V_{rad}	$\sigma(V_{rad})$	$V_{rot\,sini}$	$\sigma(V_{rot\,sini})$	$(B - V)$	V	Membership
7001	119.838542	-10.705722	50.1	0.8	18.0	0.4	0.886	14.990	NM
7002	119.839917	-10.872389	44.5	0.8	19.9	0.5	0.988	12.494	NM
7003	119.842792	-10.805722	-23.5	1.5	28.6	1.2	0.464	14.859	NM
7004	119.843833	-10.855722	61.0	0.7	17.3	0.4	0.856	14.578	NM
7005	119.845708	-10.889056	60.6	0.1	16.2	1.7	1.030	13.466	NM
7006	119.850667	-10.822389	27.0	2.6	33.2	2.0	0.322	14.689	NM
7007	119.852095	-10.891248	-13.5	1.6	51.1	1.3	0.890	11.600	NM
7008	119.852125	-10.839056	83.6	0.7	9.1	0.2	0.897	14.703	M
7009	119.855000	-10.789056	74.6	0.7	20.3	0.5	0.642	14.495	NM
7010	119.857170	-10.924294	103.7	2.3	29.2	2.7	0.394	15.210	NM
7011	119.861862	-10.760853	101.5	0.7	11.0	0.3	1.071	13.935	NM
7012	119.862495	-10.905938	69.4	0.7	11.3	0.3	1.061	13.904	NM
7013	119.862595	-10.620172	39.3	1.1	18.2	0.6	1.304	12.546	NM
7014	119.864540	-10.904671	23.1	0.6	9.7	0.2	0.600	14.529	NM
7015	119.866119	-10.894622	83.8	2.7	85.5	6.6	0.399	15.174	M
7016	119.871458	-10.939056	-45.9	1.0	14.2	0.5	0.575	14.335	NM
7017	119.872849	-10.654552	59.8	2.4	60.7	3.3	0.439	14.419	NM
7018	119.879631	-10.691129	27.0	0.5	13.7	0.2	0.873	12.398	NM
7019	119.880058	-10.631248	82.9	0.6	9.1	0.2	0.910	14.548	M
7020	119.880890	-10.916945	20.1	0.6	14.8	0.3	0.782	14.730	NM

NOTE—A short sample of lines is presented here to indicate the format and content of the full table which will be available online.

relation function, from which estimates of each star’s radial velocity are easily inferred. Rotational velocities can also be estimated from the cross correlation function full-width (CCF FWHM) using a procedure developed by [Steinhauer \(2003\)](#). This procedure exploits the relationship between the CCF FWHM, line widths and V_{sini} , using a set of numerically “spun up” standard spectra with comparable spectral types to constrain the relationship. For a significant fraction of our sample, higher rotational velocities conspired with weaker lines to produce spurious values of the radial velocity when the region near $H\alpha$ was excluded; quoted values in our table include stars for which the cross correlation included $H\alpha$. For simplicity, V_{rot} as used here implicitly includes the unknown $sini$ term.

There are two means to test the precision of the radial velocities, the size of the scatter among multiple observations of the same star and the scatter in residuals relative to an independent source of measurements. Over the multiple HYDRA runs, 36 stars were observed twice and 2 stars were observed 3 times. The dispersions in radial velocity for the latter pair are 0.70 and 0.55 km

s^{-1} . Among the stars with two observations, star 7112 showed a difference of 28 km s^{-1} between the two epochs and is clearly a double-lined spectroscopic binary. It sits among the giants at the level of the clump and undergoes eclipses ([Arentoft et al. 2007](#)). With both sets of lines visible, it is likely that the system is composed of two first-ascent red giants.

For the 35 remaining paired sets of observations, the average absolute difference in the radial velocities is 0.84 ± 0.96 km s^{-1} . However, the two pairs with the largest discrepancies, 3.22 and 4.62 km s^{-1} , are stars 1359, categorized by [Mermilliod & Mayor \(2007\)](#) as a probable binary, and 4376, tagged as a probable binary in the current investigation due to the range in published velocities for this star. If these two are removed from the sample, the mean offset between paired observations becomes 0.65 ± 0.57 km s^{-1} .

We next compare our data with that of [Mermilliod & Mayor \(2007\)](#); [Mermilliod, Mayor, & Udry \(2008\)](#), which supercedes the smaller and/or less precise samples of [Friel & Janes \(1993\)](#); [Minniti \(1995\)](#); [Carretta et al. \(2004\)](#); [Reddy, Giridhar, & Lambert \(2012\)](#), and

with the more recent work of [Carlberg \(2014\)](#); [Carlberg, Cunha, & Smith \(2016\)](#). Of the 30 members and 4 non-members observed by [Mermilliod & Mayor \(2007\)](#), all but two of the non-members and two of the members were included in our observations. For the remaining 30 stars, the mean residual in radial velocity, in the sense (MM - Table 1), is $+0.58 \pm 1.80 \text{ km s}^{-1}$. If probable binaries 1359, 2251, and 4376 are removed, the mean residual drops to $+0.31 \pm 0.96 \text{ km s}^{-1}$. It is encouraging to note that the dispersion is very comparable to that derived from a similar analysis of the giants and main sequence stars in NGC 6819 ([Lee-Brown et al. 2015](#)). Our cluster mean velocity for the 25 members is $83.2 \pm 1.2 \text{ km s}^{-1}$.

[Carlberg \(2014\)](#) has published radial velocities for 27 red giant members of NGC 2506; all but 2122 are included in the current study. From the residuals between the two samples, five stars stand out as anomalous, 2109 and 2276, as well as the already identified 1359, 2251, and 4376. If these stars are eliminated, the 21 remaining stars generate mean residuals of $+0.63 \pm 1.04$. [Carlberg \(2014\)](#) finds a mean radial velocity for these 21 giants of $+83.9 \pm 1.1 \text{ km s}^{-1}$.

Finally, [Carlberg, Cunha, & Smith \(2016\)](#) present observations of five red giants in NGC 2506, all of which were included in the three previous studies. While velocities of four of the stars are consistent with previous observations within the uncertainties, star 3265 exhibits a range from 80.3 to 85.3 km s^{-1} . While not conclusive, the spread could be indicative of a binary classification, as noted by [Carlberg, Cunha, & Smith \(2016\)](#), who also emphasize the peculiar location of this star in the CMD and the distinctly anomalous $[\text{Fe}/\text{H}]$ derived relative to the other four giants.

3. CLUSTER MEMBERSHIP

3.1. Probable Binaries

To minimize the potential distortions in any trends between main sequence and red giant stars, in addition to removing non-members, it's valuable to identify likely binaries which may have either anomalous colors and spectra, as well as modified evolution due to binary interaction. Among the giants, it has already been noted that stars 1359, 2109, 2251, 2276, 3265, and 4376 are probable binaries. [Arentoft et al. \(2007\)](#) have used intermediate-band photometry to identify a large sample of variables in the field of NGC 2506, including 3 eclipsing binaries brighter than $V = 15.6$. This sample includes the already noted giant, 7112, and two stars near the turnoff, 1136 and 1212, both of which appear to be radial-velocity cluster members based upon preliminary analysis of unpublished high resolution spectroscopy of these stars ([Arentoft et al. 2007](#)). Star

3255 (V10) is a red giant blueward of the clump with two almost identical radial-velocity measures, both consistent with cluster membership. [Arentoft et al. \(2007\)](#) find variability at the mmag level with a periodicity of 10 d^{-1} , though it does lie near the saturation limit of their photometric survey. As a member, it is clearly not a δ Scuti star.

A straightforward method for tagging potential binaries from single spectra is to look for a double set of lines within the spectrum, as revealed via *fxcor* or, at minimum, a consistent asymmetry in the line profile for a spectrum caused by the overlap of two lines. From visual and *fxcor* inspection of all the spectra, stars 1106, 2144, 2376, 3378, 4262, 5086, 7025, 7033, 7050, 7057, 7052, 7101 and both spectra for 7112 were noted as possible spectroscopic binaries.

It should be mentioned that the apparently low fraction of identified binaries ($< 10\%$) is not indicative of the probable cluster fraction and is primarily tied to the combination of selection effects in the initial selection of probable cluster members at the turnoff, the limited number of radial-velocity measures per star, and the limits on the radial-velocity measurements for stars with higher than average rotation.

3.2. Radial-Velocity Membership

With radial velocities for 287 stars but proper-motion membership for only 129, final membership for the majority of the sample is strongly dependent upon the single velocity component, weighted by location within the CMD. While this approach worked extremely well for NGC 6819 ([Lee-Brown et al. 2015](#)), the younger age by 0.4 Gyr places the turnoff of NGC 2506 in a regime where rotational speeds can remain high (greater than 25 km s^{-1}), significantly impacting the precision of the radial velocity. It should be noted that for the giants, the measured rotational velocity is dominated by the resolution of the spectra and therefore should be regarded as an upper limit to the true value. By contrast, [Carlberg \(2014\)](#) derived precision rotational velocities from $R \sim 44000$ spectra from the MIKE spectrograph. From 21 single-star members common to our sample, [Carlberg \(2014\)](#) finds an average rotational speed of $3.2 \pm 1.2 \text{ km s}^{-1}$; our lower R data generate an average of $13.8 \pm 3.0 \text{ km s}^{-1}$.

To determine membership by radial velocity alone, any star with a radial velocity more than three σ from the cluster mean as defined by our single cluster giants (83.3 km s^{-1}) will be classified as a probable non-member. To set the individual σ for each star, two factors were taken into account. First, as expected, the calculated uncertainty in the radial velocity is well correlated in approximately linear fashion with the rotational speed. We averaged the calculated error in radial

velocity as defined by $fxcor$ and the error as predicted from V_{rot} , i.e. $\sigma_{V_{rad}} = 0.044 * V_{rot} + 0.246$. Second, in the limit of perfect velocity measurements, this estimate implies no expected dispersion among the stars, ignoring the intrinsic velocity dispersion among the sample caused by motion about the center of mass of the cluster. Thus, the previously quoted dispersions among the purportedly single-star radial velocities for the red giants in our sample (1.2 km s^{-1}) and that of [Carlberg \(2014\)](#) (1.1 km s^{-1}) are combinations of both measurement errors and the intrinsic spread among the giants. The slight improvement in the dispersion for the data with higher resolution isn't unexpected so, as an approximate estimate for the intrinsic radial velocity spread, we adopt 1.0 km s^{-1} . This is effectively the same value we would get if we adopted 1.2 km s^{-1} for the total dispersion, but removed $0.6 - 0.7 \text{ km s}^{-1}$ as the instrumental scatter derived from multiple observations of the same stars over different runs. The final adopted σ in the individual V_{rad} becomes the addition in quadrature of the fixed intrinsic cluster spread with the individual measurement error as derived above.

Application of the radial velocity criterion to 265 probable non-binary stars leads to initial membership for 187 stars, though we emphasize that the claim to single-star status is based upon a lack of direct evidence for binarity, which is difficult to come by for stars with only one spectroscopic observation. Of these 187 stars, 98 have proper-motion probabilities, 86 of which are above 50%. As the second cut, we eliminate the 12 stars with probability ranging from 0% to 42%, leading to a final sample of 175 probable, single-star members. It is encouraging to note that of the 78 stars classified as radial-velocity non-members, 17 have proper-motion probabilities of which 13 lie below 50%. The distribution of single-star members (solid black line) and non-members (dashed blue curve) based solely on radial velocity is shown in Fig. 1.

3.3. The Color-Magnitude Diagram

To optimize the precision of the photometric input for the atmospheric parameters needed for the spectroscopic analysis, particularly T_{eff} from colors and $\log g$ from location within the CMD, use will be made of three photometric indices, $b - y$, $B - V$, and hk . For the color temperature, the $B - V$ values of [Van Stockum et al. \(2005, hereafter VS\)](#) defined the starting point. As a check on the photometric zero-point, comparison with the photoelectric observations of [McClure, Twarog, & Forrester \(1981\)](#) for 29 stars, 23 brighter than $V = 16.0$, led to a mean offset of -0.010 ± 0.025 , in the sense (MC - VS), which was applied to the CCD $B - V$ system.

Photometric indices from the intermediate-band (AT16) and broad-band (VS) surveys are available for

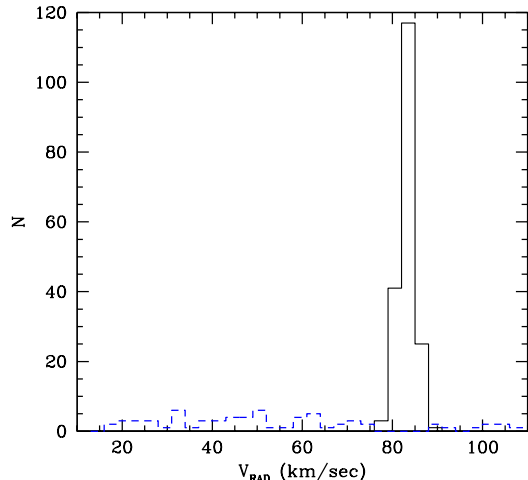


Figure 1. Distribution of radial velocities for single stars classified as probable radial-velocity members (solid black line) and potential non-members from radial-velocity alone (blue dashed line).

over 2000 stars. A cubic relation between $(b - y)$ and $(B - V)$ was determined using a set of 730 stars with the lowest color errors; the relationship has a standard deviation in $(B - V)$ color of 0.022. A similar relationship was determined between hk indices and $B - V$ using solely cool member giants (AT16) to provide an additional temperature measure.

The spectroscopic sample includes ten stars without Strömgren photometry due to placement slightly outside the field of the published Strömgren survey. For nine of these stars, the VS photometry was used exclusively. Conversely, the broad-band photometry suffered a few gaps, particularly at the very bright end. For four of the five stars lacking photometry from the VS survey, we relied exclusively on the Strömgren photometry. These few very bright stars targeted primarily the red giants, although one of the five bright stars, 1375, is clearly a hot star. For the one star lacking photometric indices from both surveys, 7007 (Tyc 5416-2526-1), Tycho values were used for V and $B - V$.

From 273 nonvariable stars in the spectroscopic survey in common with VS, the mean difference in V in the sense (AT16 - VS) is -0.009 ± 0.021 . Since the AT16 V system is in excellent agreement with that of [McClure, Twarog, & Forrester \(1981\)](#), where the mean difference in V from 33 stars brighter than $V = 17.0$ is -0.001 ± 0.034 in the sense (MC - AT16), a simple average of AT16 and VS was adopted for V . For 9 of the 10 stars not surveyed by AT16, the V magnitudes of VS were adopted without modification.

Fig. 2a shows the CMD for all stars observed spectroscopically; Fig. 2b is composed of NGC 2506 radial-

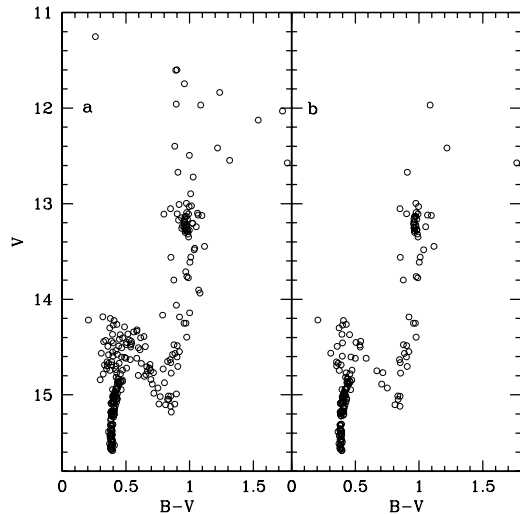


Figure 2. (a) CMD for all stars observed spectroscopically. (b) Probable single-star members of the spectroscopic sample.

velocity and, if available, proper-motion members for which no evidence of binarity currently exists. Table 1 summarizes the basic information about all stars observed spectroscopically. Stars listed as M are probable radial-velocity members, NM are nonmembers, MB are probable binary members, MN are radial-velocity members with proper-motion membership below 50%, B are probable binaries for which the radial velocity deviates significantly from the mean, and BNM and BM are binaries with deviant radial velocities but proper-motion probabilities below and above 50%, respectively.

What is apparent from a comparison of the two CMDs is that the greatest decline in stars due to the elimination of radial-velocity non-members is concentrated in two regions of the CMD. The first is near the top of the vertical turnoff, between $V = 14.2$ and 14.8 . A large sample from outside the original proper-motion survey region was selected from this region of the CMD in the hope of mapping the turnoff hook and the initial phase of evolution to the subgiant branch. The second concentration is among the red giants in the vertical band between $B - V = 0.8$ and 1.2 , where stars were initially retained in the hope of adding to the cluster subgiant and red giant branches. While some of these stars, particularly brighter than the clump, proved to be non-members, 29 probable subgiant and giants members were added to the final sample. Again, both color regions will be contaminated by field stars at any age younger than ~ 3 Gyr for the turnoff and at almost any age for disk red giants and clump stars. Since we only have one velocity component for these stars, even with relatively tight radial-velocity limits, it is probable that a handful of field non-members are still contained within the member sample.

4. METALLICITY

Determination of stellar elemental abundances from high dispersion spectroscopy depends upon a variety of factors, from the signal-to-noise ratio of the spectroscopic region under analysis to the fundamental stellar parameters defining the strength and appearance of the line profiles: V_{rot} , T_{eff} , $\log g$, and microturbulent velocity, v_t . With high resolution over an extended wavelength region and a large number of lines for both neutral and ionized elements, one can constrain the potential range of parameters by requiring a lack of trends between the derived abundances and the fundamental parameters, as well as the excitation potential. For a smaller spectral wavelength range with fewer lines, one is forced to fall back on alternative means of deriving the key parameters, independent of the spectrum, e.g. using a color-based T_{eff} and $\log g$ defined by position in the CMD for cluster members.

Since the first cluster analysis in this series for NGC 3680 (Anthony-Twarog et al. 2009), where a modest number of mostly dwarf stars and a few giants were being considered, our approach has evolved to allow discussion of samples expanded by almost an order of magnitude compared to earlier work by us and others. A key change, as exemplified by NGC 6819 (Lee-Brown et al. 2015), has been the adoption of an automated line-measurement program, ROBOSPECT (Waters & Hollek 2013), to replace exclusive dependence on manual measurement of line equivalent widths as input in traditional model atmosphere analysis via MOOG (Snedden 1973). Because ROBOSPECT consistently performed as well as manual measurements over the color range from dwarfs to giants, the primary sources of uncertainty among the final abundances within a cluster ultimately depended upon the primary parameters of T_{eff} and v_t . In theory, one could adjust these two scales for the stellar sample until the abundances showed no trend with either variable, but this would minimize the slope without supplying an independent check on the zero-point of the abundances. In particular, the color- T_{eff} relations adopted to date for the dwarfs and giants come from two independent relations, each of which has its own slope and zero-point, leading to the possibility of a mismatch between these two subsamples within the same cluster. While one could check the derived parameters against those already published for cluster stars observed at high dispersion by others, in many cases the samples only discuss either dwarfs or giants, but not both, or little if any high dispersion work is available for the cluster of interest.

As an alternative to our photometric T_{eff} values and EW-based spectroscopic $[\text{Fe}/\text{H}]$ estimates, we have attempted to derive T_{eff} and $[\text{Fe}/\text{H}]$ for each star in our

sample using ANNA (Lee-Brown 2018, in prep), a new, flexible, Python-based code for automated stellar parameterization. ANNA utilizes a feed-forward, convolutional neural network (Arbib 2002), a machine-learning technique, to infer stellar parameters of interest from input spectra. Multiple tests show that ANNA is capable of producing accurate metallicity estimates with precision competitive with our EW-based analysis. Additionally, ANNA is capable of accurately inferring T_{eff} from our spectra alone, providing an alternate temperature determination for each star. A deeper discussion of ANNA’s design and capabilities will be given in Lee-Brown (2018), but we briefly summarize its operation here. ANNA is freely available for download; the version of ANNA used in this investigation can be found at Zenodo, while the current version of the code can be found at GitHub.

4.1. ANNA: A Neural Network for Temperatures and Abundances

ANNA builds on previous studies examining the suitability of neural networks as tools to parameterize stellar spectra (e.g., Bailer-Jones et al. 1997; Allende Prieto et al. 2000; Snider et al. 2001; Manteiga et al. 2010; Dafonte et al. 2016; Li, Pan, & Duan 2017). The neural network used in ANNA consists of *layers* of sequential mathematical operations. The first, or input, layer is a stellar spectrum consisting of an ordered sequence of pixel values. These values are then summed according to many different sets of weight vectors, such that a set of weighted sums of the inputs is calculated. This collection of weighted sums forms a *hidden* layer. Each of the weighted sums in this hidden layer then serves as input to a non-linear function. In ANNA, this function is the rectified linear unit (ReLU), defined as $f(x) = \max(x, 0)$, where x denotes the weighted sum serving as input to the function. The outputs from this function are then used to construct another set of weighted summations, organized into another hidden layer, and the process repeats several times. The final result of this sequence of operations is a set of outputs $\{y_i\}$ which, in the case of ANNA, consists of the stellar parameters of interest that have been inferred from the input spectrum.

ANNA contains five layers: an input and an output layer connected via three sequential hidden layers. The first hidden layer is a convolutional layer which contains a collection of filters that are each convolved with the inputs. The filters consist of collections of weights used to construct a weighted sum that only depends on a localized subset of the layer inputs. The filters are windowed across the inputs to generate many such localized summations. This localization reduces the number of free parameters (weight values) in the first hidden layer,

helping to reduce overfitting during training while improving computational performance (see Arbib 2002). The other two hidden layers are fully-connected; each summation in these layers is connected via weights to all the ReLU operations in the previous layer.

ANNA’s ability to translate between input spectra and accurate stellar parameters requires correct selection of each weight value used during the summation steps. This selection is done automatically through supervised learning. Initially, small weight values are sampled randomly from a normal distribution. The network is then provided an input consisting of a spectrum whose output parameters are known. ANNA will produce outputs based on the input spectrum; the accuracy of these reported outputs can be quantitatively assessed via a cost function, $J(y_{\text{true}}, y_{\text{infer}})$, that measures the deviations of the reported outputs from the known stellar parameters. In ANNA, a quadratic cost function is used, $J = \Sigma(y_{\text{true}} - y_{\text{infer}})^2$. Thus, for large deviations of the network outputs from the known values, the value of J is correspondingly large. Minimization of J , therefore, implies that the networks weights are such that y_{infer} closely matches y_{true} . This minimization is accomplished by computing the gradient of J with respect to each network weight, followed by an update of the weights in the direction of lower J . Through successive iterations of this updating process, the weights eventually converge to optimal values. The network will then be capable of inferring stellar parameters from spectra whose parameterizations are unknown.

Table 2. ANNA Training Set Parameters

Parameter	Range
T_{eff} (K)	3500 to 7500
[Fe/H] (dex)	-1.0 to 0.0
$\log(g)$ (dex)	2.0 to 4.5
v_t (km s ⁻¹)	1.0 to 2.5
V_{rot} (km s ⁻¹)	0 to 70
RV (km s ⁻¹)	-10 to 95
S/N	100 to 250

We trained ANNA using continuum-normalized spectra generated with the code SPECTRUM (Gray & Corbally 1994), Kurucz atmospheric models (Kurucz 1992), and a custom linelist generated using VALD (Kupka et al. 1999) that was adjusted to reproduce the solar spectrum. We generated 15,000 high-resolution ($R \sim 670,000$) training spectra with parameters ran-

domly selected between the ranges given in Table 2. The high resolution spectra were then post-processed to better mimic our sample of HYDRA spectra. This post-processing included random radial-velocity shifts, rotational broadening, and smoothing using a Gaussian line-spread function to a resolution of $R \sim 9000$. This resolution is lower than the actual resolution of our spectra ($R \sim 13000$), and was selected during testing of ANNA as it represents the resolution corresponding to the minimum average RMS deviation between our synthetic training spectra and a sample of real Hydra spectra. This adoption of a lower-than-actual resolution for our training spectra likely indicates that our synthetic models imperfectly reproduce the line-spread function of the spectrograph and/or do not completely model the subtle broadening effects due to changes in surface gravity or microturbulent velocity. However, during testing we ultimately determined that ANNA’s temperature and metallicity determinations were relatively insensitive to the adopted training resolution; our ANNA results are materially unchanged if we were to instead adopt $R \sim 13000$ during training. This is likely due to the fact that temperature and metallicity are more sensitive to relative line strengths, rather than the particular shapes of the line profiles.

The pixel scale was set to 0.2 \AA px^{-1} . We also limited the wavelength coverage of our training spectra to $6625 \text{ \AA} - 6825 \text{ \AA}$. This was done to avoid having to model calibration artifacts in our real spectra in the region of $H\alpha$. After post-processing, our training sample consisted of 225,000 spectra.

During training, subsamples of 100 randomly selected example spectra were used during each weight update iteration. When spectra were selected for training, a wavelength-dependent amount of noise was added according to a randomly selected S/N value and a relative S/N template derived from HYDRA observations of the sun. Additionally, small, random continuum offsets were added to simulate continuum placement errors in our real spectra. Training was carried out until the network cost function failed to improve within 20,000 weight update iterations, for a total of approximately 200,000 iterations.

After training, we verified the capabilities of the trained network using a sample of real HYDRA spectra. This sample included spectra of the sun, as well as members of the open clusters NGC 6819 (Lee-Brown et al. 2015) and the Hyades (Cummings et al. 2017). These test spectra were first linearly interpolated onto the wavelength grid used during the training process. Of the potential stellar parameters, the trained network most reliably determined the correct T_{eff} and $[\text{Fe}/\text{H}]$; this is unsurprising as these two parameters contribute most strongly to the observable features in our

selected spectral range. Hotter stars in our test sample ($T_{\text{eff}} \sim 6500 \text{ K}$) could not be accurately parameterized by ANNA, likely due to a lack of strong spectral features over the wavelength range of interest. For cooler stars, we verified that ANNA returned reliable parameter determinations down to $T_{\text{eff}} \sim 4000 \text{ K}$ using NGC 6819 spectra. With the exception of one star (4402), which we omit from our ANNA analysis, the stars in our NGC 2506 sample have surface temperatures well above this tested value.

ANNA’s T_{eff} and $[\text{Fe}/\text{H}]$ results derived from the cooler ($T_{\text{eff}} \leq 6500 \text{ K}$) test spectra compare favorably with parameters known *a priori*. For a sample of 89 solar spectra of typical S/N = 200 obtained from the daytime sky with HYDRA for calibration purposes during our observing runs for NGC 2506, ANNA returns an average $T_{\text{eff}} = 5780 \pm 77 \text{ K}$ (s.d.) and average $[\text{Fe}/\text{H}] = 0.04 \pm 0.03 \text{ dex}$ (s.d.). From the rich sample of 37 giants and 184 dwarfs in NGC 6819, ANNA derives $[\text{Fe}/\text{H}] = -0.01 \pm 0.09$ (s.d.) and $[\text{Fe}/\text{H}] = -0.06 \pm 0.08$ (s.d.), respectively, in excellent agreement with the EW analysis (Lee-Brown et al. 2015) which generates $[\text{Fe}/\text{H}] = -0.03 \pm 0.09$ (s.d.). Finally, despite the Hyades’ super-solar metallicity, $[\text{Fe}/\text{H}] \sim 0.15$ (see discussion in Cummings et al. 2017), which places it outside the range of metallicities used during training, ANNA correctly infers $[\text{Fe}/\text{H}] = 0.17 \pm 0.05$ (s.d.). These results collectively indicate ANNA’s reliability over a range in stellar T_{eff} and $[\text{Fe}/\text{H}]$ typical of disk clusters.

4.2. ANNA Parameters: NGC 2506

The initial database of spectra processed through ANNA consisted of the 175 dwarfs and giants classed as single-star members, as detailed in Table 1. It quickly became apparent that the stars at the turnoff, even with T_{eff} below 6500 K, generated results which were inconsistent and/or subject to larger than desirable errors. Since the same conclusion was reached after using ROBOSPECT, independent of ANNA, and by tests using manual equivalent width measurements for a representative subset of turnoff stars, the source of the problem lies with the spectra rather than the technique adopted. In contrast with our work on NGC 6819, the fundamental weaknesses of the dwarf analyses in NGC 2506 are due to the lower metallicity of the cluster, the hotter T_{eff} due to the younger age combined with a lower metallicity, and the significantly wider range of V_{rot} . In fact, the large majority of stars at the turnoff of NGC 6819 have V_{rot} below 25 km/sec (Deliyannis et al. 2018, in prep.), in contrast with NGC 2506 where this value defines an approximate lower bound for the majority of stars at the turnoff.

We therefore used ANNA to derive T_{eff} and $[\text{Fe}/\text{H}]$ only for stars with $(B - V)_0$ between 0.65 and 1.15, ex-

cluding only one cool giant with $(B - V)_0$ greater than 1.7. The results for 62 red giant members are presented in Table 3 under the columns T_{NN} and $[\text{Fe}/\text{H}]_{NN}$. From these 62 stars, we first construct a mean $[\text{Fe}/\text{H}]$ value = -0.25 ± 0.13 (s.d.). The majority of the scatter is caused by three stars which have abundances ranging from solar to twice solar. These metallicities are consistent with those derived from ROBOSPECT measures and traditional equivalent width analyses. The implication is that these are, in fact, likely field stars with distinctly higher $[\text{Fe}/\text{H}]$ than the cluster. If these 3 stars are dropped, the revised cluster metallicity average and standard deviation from ANNA analysis becomes $[\text{Fe}/\text{H}] = -0.27 \pm 0.06$ (s.d.). The median of individual stellar $[\text{Fe}/\text{H}]$ values is robustly estimated as -0.26 ± 0.03 with an error estimate based on a median of star-by-star absolute deviations from the cluster $[\text{Fe}/\text{H}]$ value.

4.3. ROBOSPECT

In keeping with our approach to spectroscopic abundance determination for previous clusters in this program, our default scheme for determining model atmosphere input temperatures was based upon photometric color, specifically $B - V$, defined in the current investigation as the average of the observed $B - V$, $b - y$ converted to $B - V$, and, when available for cluster members, hk converted to $B - V$ for red giant members of the cluster. As noted earlier, the T_{eff} for each star had been based on two primary color-temperature calibrations.

For dwarfs, the adopted calibration is that of [Deliyannis, Steinhauer & Jeffries \(2002\)](#), consistent with previous and ongoing spectroscopic studies by this group and compared in detail with more recent T_{eff} calibrations in [Cummings et al. \(2017\)](#), namely:

$$T_{\text{eff}}(K) = 8575 - 5222.7(B - V)_0 + 1380.92(B - V)_0^2 + 701.7(B - V)_0([\text{Fe}/\text{H}] - 0.15)(1)$$

In previous investigations, the giant star color-temperature calibration of [Ramírez & Meléndez \(2005\)](#) was used for stars with $B - V > 0.5$. With the availability of the revised T_{eff} estimates produced by ANNA for subgiants and giants, we have replaced the cool-star

calibration with the newer values. To mesh the scales smoothly, the reddening-corrected $(B - V)_0$ values for dwarfs have been run through the dwarf T_{eff} calibration for all stars bluer than $(B - V)_0 = 0.34$, adopting $[\text{Fe}/\text{H}] = -0.30$. For stars redder than $(B - V)_0 = 0.7$ to $(B - V)_0 = 1.2$, we have adopted the ANNA T_{eff} values, excluding the three stars which appear to be metal-rich from both ANNA and ROBOSPECT analyses. These data were then fit with a cubic relation:

$$T_{\text{eff}}(K) = 8751.5 - 6955.7(B - V)_0 + 4519.1(B - V)_0^2 - 1461.1(B - V)_0^3 \quad (2)$$

Since the relation is tied to a specific $[\text{Fe}/\text{H}]$, it is appropriate for NGC 2506 alone.

From the 107 single-star dwarfs, the mean T_{eff} offset, in the sense (OLD - NEW), is -0.2 ± 6.5 K. For 53 giants, the analogous comparison between ANNA T_{eff} and the mean relation above is $+0.3 \pm 92.5$ K. If all giants, including the three anomalous stars, are compared, the values become $+0.7 \pm 98.9$ K.

Surface gravity estimates ($\log g$) were obtained by direct comparison of V magnitudes and $B - V$ colors to isochrones of [VandenBerg, Bergbusch, & Dowler \(2006\)](#), constructed for a scaled solar composition with $[\text{Fe}/\text{H}] = -0.29$ and an age of 1.85 Gyr, the same as the comparison presented in AT16. The isochrone's predicted magnitudes and colors were adjusted to match the cluster's reddening, $E(B - V) = 0.058$ and apparent distance modulus, 12.75 (AT16).

Input estimates for the microturbulent velocity parameter were constructed using three prescriptions. For dwarfs within appropriate limits of T_{eff} and $\log g$, the formula of [Edvardsson et al. \(1993\)](#) was used. For giants with $\log g < 3.0$, a gravity-dependent formula, $v_t = 2.0 - 0.2 \log g$, was used. For subgiants and fainter red giants, we made use of a scheme developed by [Bruntt et al. \(2012\)](#) to analyze spectra of Kepler candidate G and K stars for which T_{eff} from colors and $\log g$ validated by asteroseismology were available. The formulation by [Bruntt et al. \(2012\)](#) produces v_t estimations from a T_{eff} and $\log g$ dependent formulation that meshes well with the [Edvardsson et al. \(1993\)](#) and our previously used formula for giants if incremented by 0.2 km/sec.

Table 3. Abundances for NGC 2506 Stars

ID No.	T_{NN}	$[Fe/H]_{NN}$	$[Fe/H]_{RS}$	MAD	N_{lines}	$[Ca/H]$	$[Si/H]$	$[Ni/H]$	$\sigma([Ni/H])$	T_{phot}	$\log g$	v_t
1108	5448	-0.21	-0.13	0.14	16	0.00	-0.34	-0.32	0.11	5372	3.23	1.35
1112	4995	-0.26	-0.26	0.06	16	-0.28	-0.34	0.04	5070	2.24	1.69
1229	4821	-0.34	-0.34	0.06	16	-0.39	-0.42	0.08	4856	2.32	1.65
1301	5358	-0.29	-0.34	0.09	16	-0.19	-0.40	-0.36	0.05	5249	3.23	1.35
1320	4971	-0.26	-0.25	0.04	16	-0.29	-0.39	0.03	5051	2.43	1.62
1325	4967	-0.30	-0.29	0.07	16	-0.34	-0.42	0.02	5070	2.34	1.65
1340	5090	-0.33	-0.24	0.09	16	0.07	-0.28	-0.29	0.04	5308	3.18	1.37
1377	5489	-0.24	-0.24	0.12	16	-0.01	-0.39	-0.29	0.07	5421	3.29	1.36
2212	4824	-0.27	-0.31	0.04	15	-0.37	-0.46	0.03	4810	1.90	1.60
2255	4933	-0.31	-0.26	0.06	16	0.05	-0.37	-0.42	0.06	5063	2.72	1.51
2309	5061	-0.25	-0.29	0.04	16	-0.32	-0.40	0.04	5065	2.31	1.66
2329	5092	-0.26	-0.28	0.06	16	0.11	-0.36	-0.38	0.01	5106	2.35	1.65
2351	0.14	0.29	10	-0.06	-0.07	-0.02	0.10	7079	3.67	2.30
2364	5289	-0.24	-0.14	0.07	16	0.28	-0.26	-0.27	0.02	5377	2.28	1.73
2375	5058	-0.16	-0.30	0.07	16	-0.25	-0.41	0.02	4990	2.60	1.55
2380	5031	-0.23	-0.22	0.05	16	-0.37	-0.36	0.06	5094	2.33	1.66
2401	5015	-0.26	-0.25	0.08	16	-0.28	-0.38	0.07	5111	2.37	1.65
2402	4546	-0.34	-0.41	0.06	16	-0.27	-0.50	0.05	4504	1.90	1.60
3110	5383	-0.25	-0.24	0.15	15	0.02	-0.34	-0.31	0.05	5364	3.23	1.35
3204	5235	-0.29	-0.21	0.08	16	0.04	-0.34	-0.35	0.07	5231	2.04	1.60
3231	5022	-0.28	-0.27	0.04	16	0.04	-0.30	-0.37	0.04	5096	2.33	1.66
3243	5467	-0.21	-0.15	0.09	16	0.05	-0.41	-0.29	0.04	5437	3.23	1.35
3324	5045	-0.24	-0.24	0.05	16	-0.27	-0.36	0.03	5089	2.43	1.62
3356	5249	-0.25	-0.27	0.06	16	0.05	-0.42	-0.34	0.02	5200	2.99	1.42
3359	5067	-0.27	-0.23	0.06	16	-0.24	-0.38	0.04	5106	2.41	1.63
3392	5096	-0.27	-0.27	0.07	16	0.06	-0.35	-0.37	0.05	5166	2.32	1.69
4109	5364	-0.27	-0.24	0.07	16	0.07	-0.30	-0.41	0.06	5311	2.75	1.54
4128	5255	-0.27	-0.26	0.08	17	0.05	-0.39	-0.48	0.07	5246	2.32	1.69
4129	-0.28	0.06	5	-0.45	-0.11	-0.25	0.18	6314	3.54	1.83
4138	5030	-0.29	-0.27	0.06	16	-0.27	-0.34	0.03	5094	2.43	1.62
4143	5058	-0.22	-0.31	0.08	16	0.05	-0.34	-0.43	0.03	5077	2.43	1.62
4205	5082	-0.24	-0.21	0.09	16	-0.29	-0.34	0.04	5094	2.42	1.63
4223	-0.30	0.06	12	-0.18	-0.28	-0.43	0.13	5886	3.42	1.48
4240	4992	-0.28	-0.29	0.07	15	0.03	-0.35	-0.43	0.02	5030	2.43	1.62
4274	5168	-0.26	-0.27	0.08	16	-0.16	-0.36	0.04	5035	2.73	1.50
4372	-0.40	0.18	6	-0.54	-1.14	-0.85	0.18	6607	3.66	2.06
4528	5534	-0.19	-0.22	0.09	16	-0.05	-0.33	-0.38	0.06	5374	3.23	1.37
5249	5526	-0.34	-0.55	0.17	16	-0.50	-0.50	-0.65	0.09	5413	3.23	1.35
5271	5059	-0.26	-0.25	0.04	16	0.10	-0.36	-0.38	0.02	5108	2.38	1.64
5371	5401	-0.23	-0.18	0.07	16	-0.05	-0.46	-0.30	0.04	5385	3.27	1.36

Table 3 continued

Table 3 (*continued*)

ID No.	T_{NN}	$[Fe/H]_{NN}$	$[Fe/H]_{RS}$	MAD	N_{lines}	$[Ca/H]$	$[Si/H]$	$[Ni/H]$	$\sigma([Ni/H])$	T_{phot}	$\log g$	v_t
7008	5423	-0.28	-0.34	0.10	16	-0.05	-0.33	-0.33	0.09	5234	3.31	1.31
7019	5234	-0.26	-0.21	0.06	16	-0.06	-0.39	-0.35	0.09	5202	3.20	1.35
7023	5090	-0.25	-0.29	0.06	16	0.04	-0.35	-0.47	0.04	5068	2.40	1.63
7026	5344	-0.23	-0.34	0.06	16	-0.17	-0.31	-0.46	0.06	5065	3.12	1.36
7031	5611	-0.48	-0.43	0.17	11	-0.34	-0.34	-0.48	0.07	5744	3.42	1.41
7032	-0.18	0.22	10	-0.19	-0.13	-0.30	0.19	6161	3.65	1.64
7036	5009	-0.26	-0.23	0.07	16	-0.10	-0.36	-0.41	0.07	5051	2.42	1.62
7041	5768	0.31	0.24	0.08	16	0.28	0.31	0.06	5643	3.58	1.31
7043	5283	-0.34	-0.27	0.07	15	0.02	-0.41	-0.22	0.03	5377	3.14	1.40
7045	4736	-0.13	-0.31	0.04	15	-0.04	-0.28	0.02	4741	2.52	1.57
7048	4981	-0.28	-0.32	0.07	16	-0.30	-0.43	0.03	5021	2.27	1.67
7066	-0.05	0.20	13	-0.54	-0.38	-0.21	0.09	6761	3.70	2.30
7069	5478	0.34	0.24	0.01	15	0.27	0.08	0.09	5369	2.60	1.60
7080	5377	-0.24	-0.21	0.10	15	-0.05	-0.32	-0.38	0.10	5288	3.23	1.35
7082	5712	-0.31	-0.27	0.16	13	-0.22	-0.31	-0.38	0.19	5771	3.42	1.42
7084	4750	-0.29	-0.34	0.04	15	-0.41	-0.48	0.02	4787	2.33	1.64
7085	4959	-0.29	-0.30	0.06	16	-0.21	-0.43	0.04	4928	2.55	1.56
7086	5247	-0.37	-0.17	0.11	16	-0.13	-0.23	-0.28	0.10	5479	3.40	1.33
7088	-0.31	0.19	6	-0.31	-0.63	-0.43	0.18	6329	3.54	1.83
7093	4989	0.04	0.02	0.11	16	-0.02	-0.15	0.07	5244	3.17	1.36
7098	5099	-0.30	-0.34	0.04	15	0.01	-0.29	-0.49	0.05	5030	2.45	1.61
7099	5055	-0.25	-0.29	0.05	16	0.04	-0.31	-0.43	0.06	5042	2.45	1.61
7102	5154	-0.22	-0.27	0.06	16	-0.35	-0.38	0.02	5070	2.39	1.63
7106	4848	-0.28	-0.33	0.06	15	-0.35	-0.50	0.06	4891	2.40	1.62
7108	4959	-0.29	-0.32	0.07	16	-0.30	-0.41	0.01	5007	2.63	1.54
7114	5001	-0.33	-0.31	0.06	16	-0.07	-0.41	-0.32	0.09	5080	3.03	1.39
7117	5085	-0.24	-0.27	0.05	16	-0.33	-0.38	0.04	5051	2.42	1.62
7128	5228	-0.25	-0.24	0.07	15	-0.32	-0.34	0.02	5115	3.03	1.40

A detailed discussion and application of the ROBOSPECT software (Waters & Hollek 2013) and its optimization as applied to more than 330 stars in NGC 6819 are supplied in Lee-Brown et al. (2015). In short, our procedure consists of identification of the measurable spectroscopic absorption lines and calibration of atomic data, automated EW measurement using ROBOSPECT (Waters & Hollek 2013), atmospheric model construction using parameters (T_{eff} , $\log g$, and v_t) as described above, and chemical abundance analysis using MOOG (Snedden 1973).

Our ROBOSPECT line list is the same as used in the analysis of NGC 6819 (Lee-Brown et al. 2015) and contains 22 lines: 17 Fe I, 3 Ni I, 1 Si I, and 1 Ca I. These lines are unblended in the solar spectrum and have solar EW values in the range 10-150 mÅ, making them ideal for EW-based abundance analysis. For each line, we adopted atomic data (wavelength, excitation potential, and $\log gf$) contained in the VALD database (Kupka et al. 1999). We then modified the retrieved $\log gf$ values such that our solar EW measures reproduced the solar elemental abundances given in the 2010 version of MOOG, using a Kurucz (1992) model with 5770 K, 4.40, 1.14 km s⁻¹, and 0.00 for T_{eff} , $\log g$, v_t , and [Fe/H], respectively.

Using our calibrated line list, ROBOSPECT then iteratively determines the continuum, noise, and line components of a spectrum and reliably returns EWs that compare favorably with manual measurement of the lines. ROBOSPECT fits Gaussian line profiles, so we restrict our EW analysis to stars with projected rotation velocities $V_{\text{rot}} \leq 30$ km s⁻¹ in order to reduce systematic EW offsets due to non-Gaussian profiles. Additionally, we reject EWs greater than 150 mÅ to restrict our analysis to lines corresponding to the linear portion of the curve of growth. Finally, we discard EWs that are within 3σ of the local noise level (calculated using a 6Å window) to prevent introduction of spurious EW measurements into our analysis.

Our sample of stars processed with ROBOSPECT began with 78 spectra drawn from the sample summarized in Table 1, choosing stars with M or MN designations and rotational velocities ≤ 30 km/sec. Application of EW quality cuts left EW measures for 1022 Fe, 207 Ni, 52 Ca, and 70 Si lines out of a possible 1326, 234, 78, and 78, respectively. The majority of rejected Fe and Ni lines fell within our 3σ significance threshold, while rejected Ca measurements generally had EWs > 150 mÅ. Our EW < 150 mÅ criterion is more stringent than the EW < 200 mÅ threshold used in Lee-Brown et al. (2015), but adopting the more generous threshold does not change our abundance results. Nine of the 78 stars had fewer than five Fe lines remaining for analysis and were not included in the cluster average, as was one ad-

ditional star with a $B - V = 1.77$, T_{eff} below 4000 K, and a spectrum dominated by molecular bands. Atmospheric parameters and EW abundances for each of the remaining 68 stars are provided in Table 3.

To translate between measured EW and [A/H], we first constructed a 1-D, plane-parallel model atmosphere for each star in our final ROBOSPECT sample using the Kurucz (1992) model grid and the T_{eff} , $\log g$, and v_t values derived from our photometric observations. One star, 5270, has a temperature (7837 K) greater than supported by the model atmosphere grid and was omitted from our sample. Our atmospheric models were then used in conjunction with our EW measurements as inputs to the *abfind* MOOG routine, resulting in an [A/H] estimate for each of our measured EWs. As shown in Figs. 3 and 4, respectively, there are no apparent trends of [Fe/H] with T_{eff} or wavelength. There is, however, a serious decline in the number of turnoff stars with measurable abundances. The entire turnoff region is at $B - V < 0.5$ ($T_{\text{eff}} > 6400$ K); only a handful of turnoff stars remain in the analysis set and these have large uncertainties. The reason for this is the declining line strength with increasing T_{eff} at a metallicity less than one-half the solar value. Thus, the statistical averages are dominated by the red giants. Among the red giants, the scatter in [Fe/H] (Fig. 4) is small, but three stars (7041, 7069, 7093) appear to have approximately solar abundance or higher, distinctly higher than the cluster mean, error bars included. Since only radial-velocity membership is available for all three stars, it is plausible that all three are field interlopers. This is especially likely for 7069, a star located well blueward of the FRG branch at $(B - V) = 0.85$, $V = 13.56$. The other two stars fall along the subgiant branch and near the base of the giant branch. As a simple statistical check, if we plot the distribution of radial velocities for all red giants included in the study without *a priori* membership insight from proper motions and assume the field star histogram of Fig. 1, as defined by the red giants alone, is continuous across the radial-velocity distribution range of the cluster, the predicted number of field stars with a compatible radial velocity is found to be between 2 and 5, in excellent agreement with the three metal-rich stars identified here.

We find the cluster median iron abundance to be [Fe/H] = -0.27 ± 0.07 dex, where the reported uncertainty is the median absolute deviation (MAD). This value was calculated by computing the median [Fe/H] for each star, and then using these values to compute the median/MAD [Fe/H] for our entire sample. This reported abundance value is robust under various calculation schemes; choosing to calculate [Fe/H] by taking the median of all Fe lines or by weighting each star's contribution to the overall [Fe/H] by the number of Fe lines

measured produces nearly the same overall result. We adopt the median/MAD statistics here as our sample size is sufficiently large and these statistics are more robust against outliers, compared with using the mean/ σ statistics. In Table 3, we give the number of Fe lines measured, median and MAD for $[\text{Fe}/\text{H}]$, as well as estimates for $[\text{Ni}/\text{H}]$, $[\text{Ca}/\text{H}]$, and $[\text{Si}/\text{H}]$ for each star in our ROBOSPECT sample. The normalized MAD statistic, $\text{MADN} = 1.48 \times \text{MAD}$, can be used to approximate the standard deviation of our $[\text{Fe}/\text{H}]$ estimate. Using the MADN, we find the iron abundance for NGC 2506 to be $[\text{Fe}/\text{H}] = -0.27 \pm 0.013$ dex (s.e.m.). This result is the same as that generated by ANNA and only slightly higher than our photometric abundance estimate of $[\text{Fe}/\text{H}] = -0.32 \pm 0.03$ (AT16).

Abundances and atmospheric parameters for each of the 65 stars with ROBOSPECT-derived abundances are reported in Table 3. For most stars we present the median abundance from 5 to 17 Fe lines along with the MAD for that star. The $[\text{Ni}/\text{H}]$ abundance estimates are not based on median values for each star, since there are at most three Ni lines in our spectral region. We converted the logarithmic value for each abundance measurement to numerical values before averaging and computing the standard deviation among measurements, then converting the Ni abundance to a logarithmic $[\text{Ni}/\text{H}]$ value. The quoted error represents the effect on $[\text{Ni}/\text{H}]$ of a standard deviation added to the numerical Ni abundance value. For the sample presented in Table 3, the cluster median value of $[\text{Ca}/\text{H}]$ is -0.01 ± 0.06 , $[\text{Si}/\text{H}] = -0.33 \pm 0.05$, and $[\text{Ni}/\text{H}] = -0.38 \pm 0.05$. For the Ca and Si estimates, the quoted error is the median absolute deviation of all of the single-star abundance estimates relative to the cluster median value; for Ni, the quoted error is the median value of each star’s estimated error, as described above.

To get a handle on the impact of possible errors in the input parameters, the abundances were redetermined under the assumption that T_{eff} was altered by ± 100 K, $\log g$ by ± 0.25 and v_t by ± 0.25 km s $^{-1}$, an approach followed in our analysis of NGC 6819 [Lee-Brown et al. \(2015\)](#). Our results are similar to those presented therein: the effect of altering T_{eff} , $\log g$ and v_t by the amounts specified above is to increment the abundance $[\text{Fe}/\text{H}]$ by ± 0.06 , 0.00 and ∓ 0.06 , respectively, for stars bluer than $(B-V) = 0.8$. Increments for redder stars are similar: ± 0.06 , ∓ 0.03 and ∓ 0.06 , respectively.

4.4. Comparison to Previous Work

There have been three studies of NGC 2506 tied to high dispersion spectroscopy ([Reddy, Giridhar, & Lambert 2012](#); [Mikolaitis et al. 2011](#); [Carlberg, Cunha, & Smith 2016](#)), all using red giant samples dominated by clump stars. For the three studies sampled, the over-

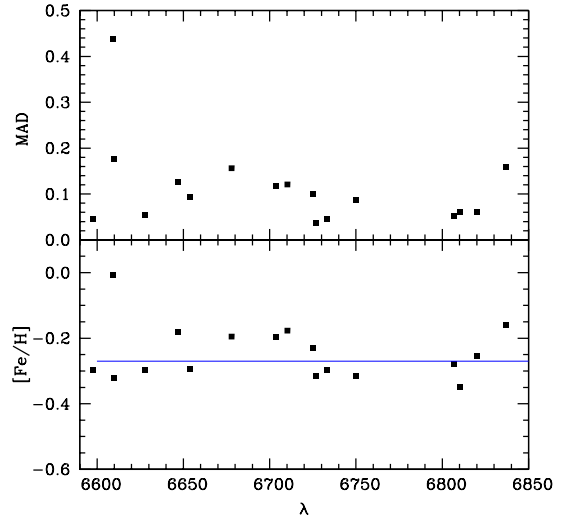


Figure 3. For each of the 17 Fe lines the abundance $[\text{Fe}/\text{H}]$ is shown as well as the MAD (median absolute deviation) for our spectroscopic sample. The blue horizontal line shows the cluster sample median value of $[\text{Fe}/\text{H}] = -0.27$.

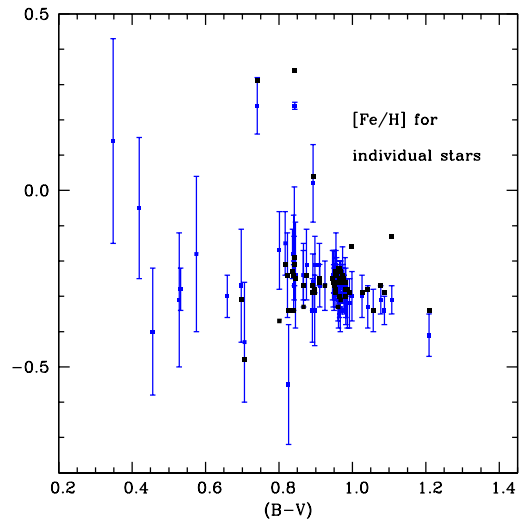


Figure 4. For each star, the median $[\text{Fe}/\text{H}]$ from ROBOSPECT analysis is shown as a function of $(B-V)$ color using blue symbols; the error bars indicate the size of the MAD statistic for that star. Black points designate $[\text{Fe}/\text{H}]$ estimates from the ANNA neural network analysis.

lap with the current investigation is 3, 2, and 4 stars; for [Carlberg, Cunha, & Smith \(2016\)](#), star 3265 was excluded due to its peculiar nature, probably a signature of binarity. In each case, we can include two T_{eff} (T_{NN} and T_{ph}) and two $[\text{Fe}/\text{H}]$ ($[\text{Fe}/\text{H}]_{\text{NN}}$ and $[\text{Fe}/\text{H}]_{\text{RS}}$) comparisons. The $[\text{Fe}/\text{H}]_{\text{RS}}$ refers to metallicity based upon analysis using the T_{ph} and equivalent widths measured by ROBOSPECT. In all three T_{eff} comparisons, the ANNA scale and the color-based scale are systematically hotter than the published values, with the color-

based T_{eff} always slightly hotter than the ANNA scale. The offsets for the two scales are $+24 \pm 96$ and $+66 \pm 63$, $+6 \pm 22$ and $+51 \pm 5$, $+19 \pm 28$ and $+63 \pm 37$, for Reddy, Giridhar, & Lambert (2012); Mikolaitis et al. (2011); Carlberg, Cunha, & Smith (2016), respectively. The analogous offsets for $[\text{Fe}/\text{H}]$ from ANNA and ROBOSPECT are -0.06 ± 0.03 and -0.07 ± 0.05 , -0.03 ± 0.07 and -0.01 ± 0.04 , and 0.03 ± 0.04 and 0.04 ± 0.04 , respectively. Since the adopted T_{eff} in the current investigation is hotter in all cases, transfer of the current data to the published systems will lower our $[\text{Fe}/\text{H}]$ in all cases, by typically 0.01 to 0.02 dex for T_{NN} and 0.03 to 0.04 dex for T_{ph} . Within the uncertainties of a small sample, this implies that we are on the same metallicity scale as Carlberg, Cunha, & Smith (2016).

For the elements other than Fe, comparisons can be made to the discussions of Mikolaitis et al. (2011); Reddy, Giridhar, & Lambert (2012). Mikolaitis et al. (2011) find $[\text{Ca}/\text{Fe}]$, $[\text{Si}/\text{Fe}]$, and $[\text{Ni}/\text{Fe}] = -0.06 \pm 0.06$, 0.01 ± 0.07 , and -0.08 ± 0.06 , respectively, while Reddy, Giridhar, & Lambert (2012) get 0.10 ± 0.05 , $+0.04 \pm 0.04$, and -0.08 ± 0.04 , respectively. Our $[\text{Ca}/\text{Fe}] = +0.28 \pm 0.07$ is based upon one generally strong line of Ca and is inconsistent with both the published spectroscopic and photometric, via the CaII-based hk index, abundances which indicate an effectively solar ratio within the uncertainties. It should be regarded as suspect. By contrast, we find $[\text{Si}/\text{Fe}] = -0.06 \pm 0.05$ and $[\text{Ni}/\text{Fe}] = -0.11 \pm 0.05$. In all three studies, Si is differentially more metal-rich than Ni by an average of $+0.09 \pm 0.04$ dex. The dominant source of uncertainty in our ratios lies with the Si abundance, tied to a single line of modest equivalent width in each star.

5. LITHIUM

5.1. Abundance Estimation

We used the SPLIT utility within IRAF to measure equivalent widths (EW) and Gaussian full-widths of the Li 6707.8 Å line for all 287 stars. A reasonably close and relatively line-free region between 6680 Å and 6690 Å was examined to estimate the signal-to-noise ratio per pixel, also estimated using SPLIT. Our analysis of the EW measurements employs a computational scheme that first numerically removes the contribution to the Li line EW produced by the nearby Fe I line at 6707.45 Å, assuming a cluster metallicity of $[\text{Fe}/\text{H}] = -0.30$ and a temperature estimate for the star. For the latter input, we used the same color-temperature scheme as described earlier. The computational scheme then interpolates within a model-atmosphere-generated grid of EWs and temperatures to estimate a Li abundance for each

star, a scheme developed by Steinhauer (2003) and employed by Steinhauer & Deliyannis (2004). A star is only considered to have a detected Li abundance if the corrected EW exceeds three times the estimated error in the EW, itself a function of the measured line width and SNR for the spectrum (Deliyannis & Pinsonneault 1993; Deliyannis, Pinsonneault, & Duncan 1993). For stars with EW below this criterion, the Li abundance can only be characterized as an upper limit and no abundance error is estimated. The abundance error estimate for detected lines is primarily dependent on the error in the EW. We did test the sensitivity of the computed Li abundance to increments of +100 K in T_{eff} . A higher T_{eff} results in higher Li abundance but by widely different amounts for different classes of stars; for warmer dwarfs, the abundance increment is ≤ 0.1 , rising to 0.15 for cooler subgiants and high sensitivity (≥ 0.3) for stars on the red giant branch.

A more subtle concern for the coolest stars arises from the presence of CN lines in the region of the Li line. From synthetic spectra, we find that at the metallicity of NGC 2506 and plausible levels of CN enhancement, the molecular lines have no impact on the measured EW. For stars of solar metallicity and higher, CN-enhanced giants can be affected.

Of the 175 stars classed as single-star members, Li detections or upper limits were possible for all but 30. Of the 30 stars, one is 4402, the coolest red giant member of our sample with $B - V = 1.76$. The confusion and complexity of features near the Li line made any attempt at a Li abundance estimate for this star impossible. This internal photoelectric standard (McClure, Twarog, & Forrester 1981) lies outside the astrometric survey (Chiu & van Altena 1981) and, like 2402, has generally been ignored in spectroscopic surveys of the red giant branch. Its location in the CMD, however, places this star closest to the tip of the red giant branch and a potential candidate for evidence of Li-enrichment (Carlberg, Cunha, & Smith 2016); observation at a higher resolution could prove informative.

The 29 remaining stars fall within a well-defined group: rapidly rotating stars ($V_{\text{rot}} > 30 \text{ km s}^{-1}$) at the CMD turnoff. The average measured rotation speed for the excluded stars is 54.2 km s^{-1} , broadening the Li line, if one exists, to a level where, when combined with the statistical noise, any attempt at directly measuring or even placing a constraint on the Li value proved implausible. The $A(\text{Li})$ values with non-zero uncertainties for stars with measureable Li and zero for stars with upper limits are presented in Table 4.

Table 4. Lithium Abundances for NGC 2506 Stars

ID No.	T _{eff}	EW(Li)	SNR	FWHM	A(Li)	σ_{ALi}	Code
1108	5372	21.2	124	0.46	0.70	0.00	2
1112	5070	16.6	129	0.80	0.55	0.00	3
1127	6909	5.0	132	0.70	2.50	0.00	1
1134	6950	30.5	158	1.60	2.94	0.09	0
1211	7004	30.0	195	1.01	2.96	0.06	0
1229	4856	53.7	124	0.67	1.11	0.06	0
1301	5249	45.9	118	0.89	1.56	0.08	0
1302	6950	23.0	117	0.90	2.80	0.12	0
1305	7009	29.9	187	1.03	2.97	0.06	0
1320	5051	13.6	143	0.64	0.55	0.00	3
1325	5070	10.9	138	0.53	0.55	0.00	3
1331	6652	45.4	155	0.94	2.94	0.05	0
1340	5308	27.0	179	0.67	1.24	0.10	0
1350	6936	56.2	170	1.94	3.25	0.05	0
1354	6968	41.0	120	0.98	3.10	0.07	0
1358	6852	34.6	198	2.04	2.94	0.07	0
1377	5421	37.1	180	0.65	1.64	0.06	0
1379	6959	27.8	175	1.10	2.90	0.07	0
1384	6735	67.4	236	2.42	3.21	0.04	0
1390	6936	5.0	140	0.70	2.49	0.00	1
1394	6702	71.4	130	1.50	3.23	0.05	0
2102	6847	44.0	188	2.30	3.06	0.07	0
2140	6856	30.2	170	0.82	2.87	0.06	0
2212	4810	26.1	96	0.68	0.40	0.00	3
2217	6635	79.2	160	1.66	3.24	0.04	0
2255	5063	39.4	147	0.72	1.18	0.08	0
2306	6963	49.0	113	1.31	3.19	0.08	0
2309	5065	9.4	145	0.58	0.55	0.00	3
2311	6640	66.5	156	1.59	3.14	0.05	0
2325	6968	5.0	100	0.70	2.67	0.00	1
2328	6860	70.2	199	2.90	3.32	0.05	0
2329	5106	12.4	156	0.56	0.55	0.00	3
2332	6869	8.2	148	0.97	2.49	0.00	1
2343	6945	32.7	94	0.70	2.97	0.09	0
2347	6865	36.0	229	1.62	2.96	0.05	0
2351	7079	52.2	250	1.50	3.30	0.03	0
2364	5377	20.5	169	0.85	0.70	0.00	2
2371	6927	32.5	174	1.02	2.95	0.06	0
2373	6963	23.6	130	1.03	2.82	0.11	0

Table 4 continued

Table 4 (*continued*)

ID No.	T_{eff}	EW(Li)	SNR	FWHM	A(Li)	σ_{ALi}	Code
2375	4990	52.2	146	0.77	1.29	0.06	0
2380	5094	16.4	175	0.81	0.55	0.00	3
2386	6945	39.9	206	1.25	3.07	0.05	0
2394	7000	37.8	122	1.29	3.08	0.09	0
2401	5111	17.4	163	0.75	0.55	0.00	3
2402	4505	60.4	94	0.71	0.59	0.10	0
3110	5364	25.0	159	0.68	1.26	0.13	0
3112	7046	25.0	103	1.03	2.90	0.13	0
3135	6891	32.8	115	1.10	2.94	0.10	0
3158	6765	65.0	115	0.67	3.21	0.04	0
3204	5231	9.2	145	0.66	0.70	0.00	3
3206	6740	45.4	199	2.25	3.00	0.06	0
3231	5096	12.4	142	0.59	0.55	0.00	3
3263	6896	26.8	176	1.20	2.84	0.08	0
3324	5089	15.6	146	0.62	0.55	0.00	3
3344	6991	44.6	134	1.10	3.16	0.06	0
3350	6918	52.7	174	1.59	3.20	0.05	0
3356	5200	36.2	160	0.75	1.32	0.08	0
3359	5106	12.5	164	0.61	0.55	0.00	3
3360	6778	76.0	194	1.72	3.31	0.04	0
3367	6968	24.2	160	1.00	2.84	0.09	0
3373	6986	30.6	109	0.89	2.96	0.10	0
3394	6927	5.0	155	0.70	2.43	0.00	1
4105	7051	23.4	138	1.33	2.87	0.12	0
4106	6887	5.0	157	0.70	2.40	0.00	1
4109	5311	31.8	180	0.68	1.38	0.08	0
4128	5246	61.4	177	0.67	1.75	0.03	0
4129	6314	64.6	118	0.98	2.88	0.05	0
4138	5094	20.6	172	0.82	0.55	0.00	2
4145	6959	21.8	120	0.88	2.78	0.12	0
4205	5094	19.7	162	0.90	0.55	0.00	2
4216	6731	74.8	195	1.56	3.27	0.04	0
4218	7327	30.6	161	0.98	3.18	0.07	0
4223	5886	60.8	200	0.77	2.48	0.03	0
4240	5030	13.5	119	0.70	0.55	0.00	3
4274	5035	37.4	160	0.92	1.09	0.09	0
4331	6883	61.4	198	2.78	3.26	0.05	0
4337	6575	84.4	170	1.88	3.24	0.04	0
4353	6968	26.8	145	0.99	2.89	0.09	0
4361	6635	43.2	213	1.88	2.90	0.05	0
4372	6607	53.1	188	1.13	2.99	0.04	0
4528	5374	38.8	160	0.69	1.62	0.06	0

Table 4 continued

Table 4 (*continued*)

ID No.	T_{eff}	EW(Li)	SNR	FWHM	A(Li)	σ_{ALi}	Code
5196	6977	32.0	148	1.35	2.98	0.08	0
5214	6453	69.5	208	1.50	3.03	0.03	0
5233	6909	58.2	190	1.61	3.25	0.04	0
5249	5413	28.8	145	0.77	1.46	0.10	0
5270	7600	5.0	230	0.70	2.69	0.00	1
5271	5108	13.5	144	0.65	0.55	0.00	3
5371	5385	5.0	135	0.70	0.70	0.00	3
7008	5234	19.3	138	0.97	0.70	0.00	3
7015	6847	41.4	180	1.58	3.02	0.06	0
7019	5202	33.7	159	0.64	1.27	0.07	0
7022	6852	49.0	200	3.82	3.11	0.07	0
7023	5068	17.3	159	0.63	0.55	0.00	3
7026	5065	38.8	145	0.67	1.17	0.08	0
7031	5744	76.0	200	0.89	2.47	0.03	0
7032	6161	74.2	193	0.99	2.84	0.03	0
7035	6472	71.6	165	0.99	3.07	0.03	0
7036	5051	18.3	129	0.59	0.55	0.00	3
7038	6786	67.8	165	2.44	3.25	0.06	0
7041	5643	66.2	129	0.77	2.27	0.04	0
7042	6765	55.4	185	1.46	3.12	0.04	0
7043	5377	46.4	124	0.78	1.74	0.07	0
7045	4741	21.9	89	0.63	0.20	0.00	3
7047	6968	36.0	140	1.12	3.03	0.07	0
7048	5021	17.9	150	0.84	0.55	0.00	3
7053	6896	46.7	177	1.21	3.12	0.05	0
7058	6932	30.3	151	1.10	2.92	0.08	0
7059	6923	65.6	173	3.24	3.32	0.06	0
7061	6689	6.0	198	0.70	2.16	0.00	1
7062	6830	5.0	230	0.70	2.18	0.00	1
7063	6744	51.0	195	2.01	3.06	0.05	0
7064	6941	40.5	157	1.16	3.07	0.06	0
7066	6761	9.0	261	0.50	2.23	0.10	0
7069	5369	30.7	105	0.75	1.44	0.14	0
7071	7107	34.6	125	1.80	3.10	0.11	0
7076	6808	48.2	125	1.55	3.08	0.08	0
7080	5288	26.4	186	0.64	1.19	0.10	0
7081	6905	24.4	164	0.86	2.80	0.08	0
7082	5771	54.7	189	0.68	2.29	0.03	0
7084	4787	28.3	120	0.64	0.20	0.00	2
7085	4928	55.6	168	0.77	1.25	0.05	0
7086	5479	51.9	140	0.95	1.93	0.06	0

Table 4 continued

Table 4 (*continued*)

ID No.	T_{eff}	EW(Li)	SNR	FWHM	A(Li)	σ_{ALi}	Code
7088	6329	73.0	156	0.87	2.97	0.03	0
7089	6673	66.0	242	2.71	3.16	0.04	0
7090	6950	45.4	162	1.11	3.14	0.05	0
7093	5244	25.4	124	0.98	0.70	0.00	2
7094	6778	49.0	193	1.18	3.06	0.04	0
7097	6619	38.8	201	1.82	2.84	0.06	0
7098	5030	10.2	176	0.69	0.55	0.00	3
7099	5042	20.4	146	0.82	0.55	0.00	2
7102	5070	17.0	156	0.78	0.55	0.00	3
7104	6757	46.6	192	1.38	3.02	0.05	0
7105	6918	67.7	143	1.73	3.34	0.05	0
7106	4891	55.0	127	0.69	1.19	0.06	0
7108	5007	41.8	155	0.73	1.15	0.07	0
7109	6900	24.6	132	1.42	2.80	0.12	0
7110	6923	5.0	118	0.70	2.56	0.00	1
7111	6972	16.1	191	1.09	2.65	0.11	0
7114	5080	12.8	180	0.64	0.55	0.00	3
7115	7102	32.0	116	0.61	3.06	0.07	0
7117	5051	22.8	165	0.79	0.55	0.00	2
7123	6727	58.2	232	0.91	3.12	0.03	0
7125	6865	24.8	155	1.20	2.78	0.09	0
7128	5115	39.7	180	0.76	1.27	0.06	0
7132	6843	62.8	169	2.18	3.24	0.05	0

NOTE—Lithium abundance values with non-zero errors (code 0) are detections; stars with abundance codes 1, 2 or 3 are upper limits constrained by SNR, the temperature grid, or both, respectively.

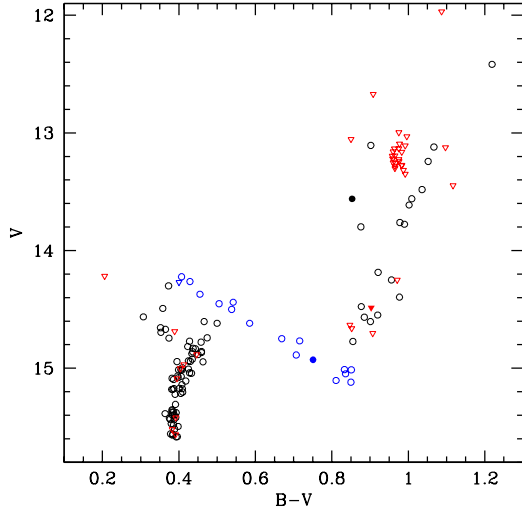


Figure 5. CMD for single-star members with detectable Li (open black circles) and upper limits to A(Li) (open red triangles). Blues stars identify the location of purported members of the subgiant branch. Filled symbols identify the three stars with estimated metallicities significantly higher than the cluster.

5.2. Evolution in the CMD

For the remaining 145 stars, Fig. 5 shows the CMD for stars with Li determinations; open black circles are detections while open red triangles designate upper limits. Blue symbols are detections for stars classed as subgiants, allowing one to uniquely distinguish these stars from turnoff stars of the same B-V but at fainter magnitudes and from stars classed as FRGs in later figures. Filled symbols identify the three stars which are spectroscopically determined to be metal-rich and therefore likely field stars, two of which have Li detections while the third has only an upper limit. Of the 41 stars with only upper limits to A(Li), 10 are located at the turnoff (defined as $B - V < 0.5$, irrespective of V) and 31 populate the giant region ($B - V > 0.8$). Among the redder stars, the sample splits into two distinct groups, stars at the base of the vertical turnup of the red giant branch and the red giant clump stars. With the exception of one anomalously blue clump star (4128), every giant located within the CMD region associated with the red clump has, at best, an upper limit for A(Li). It is crucial to note that this is not simply an issue of the clump stars exhibiting lower B-V and higher than average T_{eff} compared to FRGs at the same magnitude level and therefore weaker lines. The pattern among FRGs at the same T_{eff} but positioned 0.5 mag fainter than the red clump clearly demonstrates that if the clump stars had A(Li) similar to the FRGs, it should be detectable.

To probe the empirical trends among A(Li), we show in Fig. 6 the variation in A(Li) as a function of V . Symbols have the same meaning as in Fig. 5. The pattern

with decreasing V is a clear reflection of the evolution from the main sequence to the giant branch, with the apparent reversal between $V = 15.2$ and 14.6 caused by the shape of the subgiant branch. The stars at the turnoff, irrespective of magnitude, show an approximately constant mean A(Li) near 3.05 with a range approaching ± 0.30 dex. A(Li) steadily declines across the subgiant branch, up to the base of the FRG branch, with every subgiant having detectable Li, rather than just an upper limit. Between the base of the FRG at $V = 14.5$ and the approximate luminosity level of the red giant clump at $V = 13.0$, A(Li) among the stars with detectable Li remains effectively constant near A(Li) = 1.25. Only one star (2402) above the clump level has measurable Li, with A(Li) just below 0.6. As a newly identified probable member of the cluster, this star plays a unique role in redefining the location of the luminous end of the FRG branch. Previous discussions (Carretta et al, 2004; Mikolaitis et al. 2011; Reddy, Giridhar, & Lambert 2012) have assumed that the FRG branch above the clump passed through the positions occupied by stars 2212 ($(B - V) = 1.09$, $V = 11.97$) and 2122 (1.10, 11.7)(not included in the figure). The former star, included in this analysis, only has an upper limit to A(Li), as expected if it is a post-He-flash star. (But see the discussion on star 4128, below, on the possibility of Li production by post-He-flash stars.) If 2402 is truly a cluster member defining the FRG branch, then 2212 and 2122 lie almost a magnitude above this extension and cannot be normal, single stars in this same phase of evolution, i.e. they cannot be FRGs.

The fact that Li is detectable in 2402 at a level comparable to that found as an upper limit among the bluer and fainter clump stars is due in part to its having the coolest T_{eff} of any star with a measurable spectrum included in the membership sample. However, if its proposed evolutionary state is correct, it could be evidence that A(Li) does decline among FRGs beyond the level of the clump and prior to the He-flash, a point returned to below.

One star (4128) near $V = 13.1$ has A(Li) = 1.75, higher than the average of 1.25 for FRG stars over a range in luminosity. It is located in Fig. 5 blueward of the red giant clump, leading to potential classification as a Li-rich giant since it sits just above the relatively fluid boundary used to define such stars (e.g., Kumar, Reddy, & Lambert 2011; Silva Aguirre et al. 2014; Casey et al. 2016; Takeda & Tajitsu 2017). From isochrone comparisons (VandenBerg, Bergbusch, & Dowler 2006), the initial mass of the stars populating the giant branch in NGC 2506 is between 1.6 and 1.7 M_{\odot} . A(Li) ~ 1.5 is what standard models predict for a star of 1.5 M_{\odot} and solar abundance after the first dredge-up (Palmerini et al. 2011), but not for post He-flash red giants. Em-

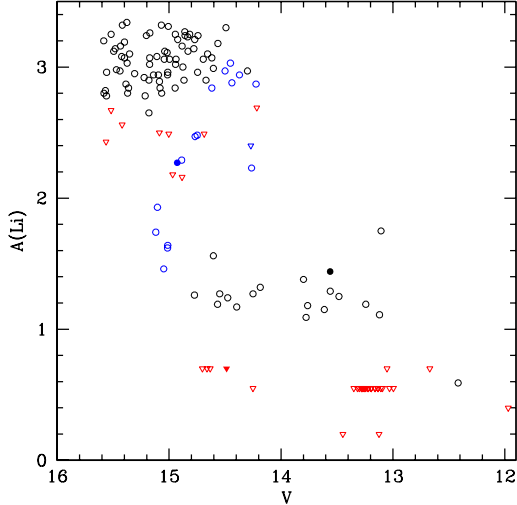


Figure 6. Li abundance as a function of V . Symbols have the same meaning as in Fig.5.

pirically, however, the star has $A(\text{Li}) \sim 0.5$ dex above the observed value for the FRGs, irrespective of the predictions of standard models, which may be a signature of actual Li production in a star in the post-He-core-flash phase (Silva Aguirre et al. 2014; Monaco et al. 2014). No other star on the giant branch, above or below the clump, exhibits Li sufficiently high enough to be tagged as a potential Li-rich star, though this is not unexpected given the often quoted 1% rate of detection for these stars in the general population of red giants.

A clearer vision of the evolutionary path is shown in Fig. 7, where $A(\text{Li})$ is plotted as a function of the $B - V$ color. For stars at the turnoff, there is again no trend of measured $A(\text{Li})$ with color between $B - V = 0.3$ and 0.5 . However, once the stars initiate evolution across the subgiant branch, there is a steady decline to a typical detection value near $A(\text{Li}) \sim 1.25$, followed by no significant decline from the base of the giant branch to the level of the clump. With the exception of only 4128, all stars readily identifiable as post-He-flash red giants exhibit only upper limits to $A(\text{Li})$.

What can we learn from these patterns, especially in light of the predictions from standard stellar evolution models? Beginning with the turnoff, there are 72 stars with $B - V \leq 0.50$ with detectable Li. The average $A(\text{Li})$ for these stars is 3.04 ± 0.19 (s.d.) dex; if one extreme outlier with $A(\text{Li}) = 2.23$ is excluded, the average becomes 3.05 ± 0.16 (s.d.); the dispersion is more than double the value of 0.07 derived from the average standard deviation as defined by the precision of the individual measures. The stars at the turnoff of NGC 2506 started on the unevolved main sequence hotter than the Li-dip, which is located at a fainter V than accessed by the spectroscopic sample. Under standard stellar evolu-

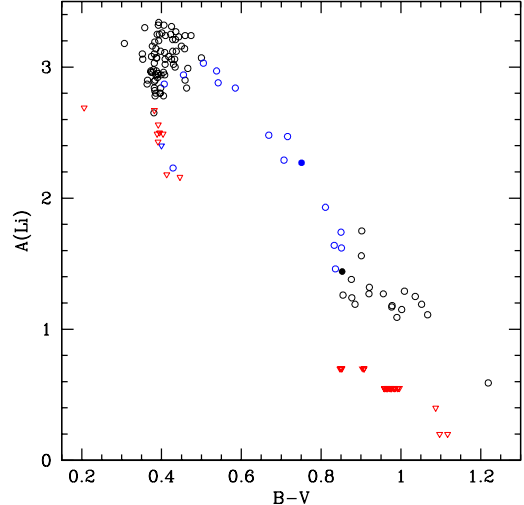


Figure 7. Li abundance as a function of $B - V$. Symbols have the same meaning as in Fig.5.

tion models, the turnoff stars should retain their initial $A(\text{Li})$ until they evolve to $T_{\text{eff}} < 5600$ K, the site of the first signature of the first-dredge-up (FDU) phase, equivalent to $(B - V) \sim 0.75$ for the subgiant stars in NGC 2506, i.e. until one reaches the reddest stars on the subgiant branch (blue symbols) at the base of the vertical FRG branch (e.g., Pinsonneault 1997; Charbonnel & Lagarde 2010).

5.3. Initial Conditions: The Primordial Cluster Li Abundance

While it is generally agreed that the location of the Li-dip is purely temperature-dependent, leading to mass ranges for the Li-dip strongly correlated with $[\text{Fe}/\text{H}]$ (Balachandran 1995; Chen et al. 2001; Anthony-Twarog et al. 2009; Cummings et al. 2012; Ramírez et al. 2012), a distinctly different question is the evolution of the Li abundance with time and $[\text{Fe}/\text{H}]$ within the Galaxy. Did clusters with lower $[\text{Fe}/\text{H}]$ form with a lower initial $A(\text{Li})$ or is the time of formation the determining factor? This question is independent of the discrepancy between the Li abundance among globular cluster stars and the primordial estimate from cosmology (Coc, Uzan, & Vangioni 2014) since both lie at $A(\text{Li}) = 2.7$ or less, well below the solar system (Asplund et al. 2009) and young cluster estimate of ~ 3.3 (Jones et al. 1997; Steinhauer & Deliyannis 2004; Balachandran, Mallik, & Lambert 2010; Cummings et al. 2017). The relevance for the current discussion is that the determination of the physical processes producing a spread of 0.6 dex in $A(\text{Li})$ among the stars at the turnoff will be heavily weighted by whether the current observed upper bound in $A(\text{Li})$ was the initial cluster value and all deviations from that value are due to Li depletions

or the primordial cluster value was lower and the spread is a combination of both enhancements and depletions of Li relative to the mean.

The difficulty in defining the original cluster value arises from the fact that for stars within the Li-dip and cooler, $A(\text{Li})$ declines over time once stars have reached the main sequence. While the rate of decline will vary with T_{eff} , with hotter stars on the red side of the Li-dip depleting at a slower rate, unless stars are observed relatively soon after attaining the main sequence, the observed abundance supplies only a lower bound. This approach has been adopted by investigations attempting to link globular cluster Li observations to the disk clusters and field stars as in Dobrovolskas et al. (2014) or from analyses of field star samples of the thin and thick disk, as recently exemplified by Fu et al. (2017). While such discussions invariably conclude that $A(\text{Li})$ has grown between the formation of the metal-deficient globulars and the current disk, the relative role of age versus metallicity in defining the growth remains obscure. As already noted, open cluster studies demonstrate that $A(\text{Li})$ depletion for stars cooler than 6500 K is a strong function of temperature and age, even for stars populating the Li plateau redward of the Li-dip (Cummings et al. 2012). The discussion by Fu et al. (2017), as an example, derives the trend of $A(\text{Li})$ with $[\text{Fe}/\text{H}]$ by averaging the 6 most Li-rich stars in each metallicity bin from a sample of ~ 300 stars ranging in $[\text{Fe}/\text{H}]$ from -1 to +0.5, sorted into thick and thin disk components based upon $[\alpha/\text{Fe}]$ as a function of $[\text{Fe}/\text{H}]$. The stars with the highest measured $A(\text{Li})$ come from a T_{eff} range of 6500 K to ~ 5500 K. The sample includes stars from the unevolved main sequence to the subgiant branch. Without knowing (a) the selection biases within the original sample, (b) the sensitivity of the results to the exact choice of the thick/thin disk boundary, a strong function of $[\text{Fe}/\text{H}]$, and (c) the exact T_{eff} and age distribution for each star used in defining the upper bound with age, the significance of their derived trend remains questionable. Since no $[\text{Fe}/\text{H}]$ bin attains an $A(\text{Li})$ upper limit above 2.85, it is clear that the dominant majority of the sample has depleted $A(\text{Li})$ from whatever value they formed with to their current level and attempting to predict the original value which defines the trend with age or $[\text{Fe}/\text{H}]$ becomes a futile and inherently biased exercise.

From standard stellar evolution theory (SSET), the solution to this constraint would be to observe stars hotter than the Li-dip since these stars should undergo no depletion because their convective atmospheres are thin to non-existent.

The obvious problem with this approach to testing the evolution of $A(\text{Li})$ with age in the Galaxy is that, except for star clusters with metallicities well below solar, by an age of 3-4 Gyr the majority of stars hotter than

the Li-dip have evolved off the main sequence and Li-dip stars are populating the turnoff region, as illustrated by M67 and NGC 6253 (Cummings et al. 2012) and Ber 32 (Randich et al. 2009). This clearly mass-dependent transition from stars with *normal* Li abundance on the main sequence to those which are guaranteed to leave the main sequence already exceptionally depleted in Li makes comparisons between the giant branches of clusters younger than ~ 2.5 Gyr with those older than this (the exact boundary is, again, metallicity-dependent) generally meaningless without first renormalizing the Li scale for the older, lower mass stars.

A cluster which is more metal-poor than NGC 2506 with $[\text{Fe}/\text{H}] \sim -0.5$ and somewhat older (3-4 Gyr) is NGC 2243 (Anthony-Twarog et al. 2005; Vandenberg, Bergbusch, & Dowler 2006; Jacobson, Friel, & Pilachowski 2011; Francois et al. 2013). Unfortunately, the cluster sits tantalizing close to the boundary where the hot edge of the Li-dip is barely contained within the turnoff region. The majority of the stars with published $A(\text{Li})$ (Hill & Pasquini 2000; Francois et al. 2013) approaching the top of the turnoff have only upper limits to their $A(\text{Li})$, as expected for Li-dip stars. There are, however, 5 stars extending toward the subgiant branch which have measurable Li, with values ranging from $A(\text{Li}) = 2.92$ to 2.39, leading Francois et al. (2013) to adopt $A(\text{Li}) = 2.7 \pm 0.2$ as the primordial Li abundance of the cluster. If, instead, the two largest values are adopted as indicative of the original cluster abundance, $A(\text{Li}) = 2.9$. Preliminary analysis of a much larger sample of turnoff and subgiant spectra obtained with HYDRA during the same observing cycle as NGC 2506 extends the detection limit for turnoff members of NGC 2243 to $A(\text{Li})$ above 3.0, with the majority of stars covering the range between 2.8 and 2.3. Statistical issues aside, since NGC 2243 is both older and more metal-poor than NGC 2506, the apparent reduced Li boundary for the hot side of the turnoff doesn't supply any insight into which parameter, time of formation or metallicity, has greater influence on the primordial $A(\text{Li})$ value.

A similar problem applies to the more metal-rich ($[\text{Fe}/\text{H}] = -0.02$ (Lee-Brown et al. 2015)) cluster, NGC 6819, with an age of 2.25 Gyr (Deliyannis et al. 2018, in prep.). Although it is much closer in age to NGC 2506 than NGC 2243, the higher metallicity places the Li-dip at a higher mass than in NGC 2506, and thus the stars brighter than the Li-dip are, on average, more evolved than the stars brighter than the Li-dip in NGC 2506. The apparent result is that the stars brighter than the Li-dip at the turnoff in NGC 6819 exhibit a much wider range of $A(\text{Li})$ than found among the turnoff stars in NGC 2506. As we will discuss below, the significant spread, from an upper limit for single stars of $A(\text{Li}) =$

3.2 to detections below $A(\text{Li}) = 2.0$, and non-detections for a majority of the stars, is a clear indication that some parameter other than T_{eff} must serve as a catalyst for Li-depletion upon leaving the main sequence.

Perhaps the best analog to NGC 2506 is IC 4651, a cluster consistently observed through both photometry and spectroscopy to be above solar metallicity with $[\text{Fe}/\text{H}]$ typically between +0.10 and +0.15 (Anthony-Twarog & Twarog 2000; Meibom, Andersen, & Nordström 2002; Pasquini et al. 2004; Carretta et al. 2004; Santos et al. 2009). Its younger age than NGC 2506 compensates in part for the shift to higher mass for the location of the Li-dip, placing the stars near the turnoff in a position relative to the Li-dip similar to that of NGC 2506. The turnoff region of the cluster is tight and well-defined, as in NGC 2506, and it is one of the few clusters in the 1-2 Gyr age range to have a few stars populate the subgiant branch just beyond the turnoff. While the sample of stars observed for Li (and Be) to date is modest (Balachandran, Anthony-Twarog & Twarog 1991; Pasquini et al. 2004; Smiljanic et al. 2010), the composite Li data for the cluster at higher mass than the Li-dip show a maximum $A(\text{Li})$ between 3.3 and 3.4 before dropping precipitously across the subgiant branch (see Fig. 9 of Anthony-Twarog et al. (2009)). Unfortunately, the full range of stars at the turnoff brighter than the Li-dip extends down to $A(\text{Li}) \sim 2.5$, a spread confirmed using the composite sample from NGC 752, NGC 3680, and IC 4651 (Anthony-Twarog et al. 2009).

Looking to clusters younger and more metal-rich than NGC 2506, the obvious choices are the virtually identical clusters, the Hyades and Praesepe, as recently investigated by Cummings et al. (2017). With $[\text{Fe}/\text{H}] = +0.15$ and ages less than 1 Gyr, the combined sample should provide a reasonable test of any correlation between $A(\text{Li})$ and $[\text{Fe}/\text{H}]$ at a given T_{eff} or main sequence mass. As illustrated in Fig. 13 of Cummings et al. (2017), from the small composite sample using only single-star cluster members, $A(\text{Li})$ does rise to a plateau value of $A(\text{Li}) \sim 3.3$ just hotter than the Li-dip boundary. Among the hotter A stars, however, the Li abundance declines, reaching $A(\text{Li}) \sim 2.5$.

Perhaps the best evidence for a Li-Fe correlation comes from an analysis of Hyades-age clusters ranging in $[\text{Fe}/\text{H}]$ from +0.15 to -0.23 by Cummings (2008). In addition to the already mentioned Hyades and Praesepe sample at $[\text{Fe}/\text{H}] = +0.15$, $A(\text{Li})$ as a function of T_{eff} from ~ 7000 K to 4500 K was measured for a large sample of stars in NGC 2539 ($[\text{Fe}/\text{H}] = 0.00$), IC 4756 ($[\text{Fe}/\text{H}] = -0.10$), NGC 6633 ($[\text{Fe}/\text{H}] = -0.10$), and M36 ($[\text{Fe}/\text{H}] = -0.23$). Each cluster exhibited a well-defined trend between $A(\text{Li})$ and T_{eff} , with virtually identical patterns for paired clusters of the same metallicity. However, when the relations at the three metallicities were su-

perposed, they had distinctly different zero-points and slopes. For $T_{\text{eff}} > 5700$ K, $A(\text{Li})$ declined with decreasing $[\text{Fe}/\text{H}]$ while for the cooler sample, the pattern reversed. The solution to the contradiction with the theoretical prediction from main sequence models with mixing due to convection is twofold: first, adopt a primordial cluster $A(\text{Li})$ strongly correlated with $[\text{Fe}/\text{H}]$, i.e. the Hyades and Praesepe formed with $A(\text{Li})$ higher than that found in IC 4756 and NGC 6633 by ~ 0.3 dex. Based upon the relation derived from cluster data (Cummings 2008), a straightforward, unweighted linear fit between $A(\text{Li})$ and $[\text{Fe}/\text{H}]$ over the $[\text{Fe}/\text{H}]$ range from -0.2 to +0.1 gives:

$$A(\text{Li}) = 3.315 \pm 0.003 + 0.959 \pm 0.034[\text{Fe}/\text{H}]$$

One would expect a cluster with $[\text{Fe}/\text{H}] = -0.27$ like NGC 2506 to have a primordial value of $A(\text{Li}) = 3.06$, consistent with the mean value observed among the turnoff stars more massive than the Li-dip. Second, for stars cooler than the Li-dip, the rate of Li destruction at a given T_{eff} is metallicity dependent, with more metal-rich clusters exhibiting higher rates of depletion.

Collectively, the evidence points (a) with high probability to the fact that the scatter in $A(\text{Li})$ among the stars at the cluster turnoff is real and a product of evolution on the main sequence and (b) to the possibility that the lower mean cluster Li abundance in NGC 2506 ($A(\text{Li}) = 3.0$) compared with clusters with more Hyades-like metallicity ($A(\text{Li}) = 3.4$) is real and is tied to the intrinsically lower $[\text{Fe}/\text{H}]$ of the former. Just how much NGC 2506 and NGC 2243 lie below the more metal-rich objects ultimately depends on how one weights the wide distribution of $A(\text{Li})$ found among the sample of stars more massive than the Li-dip when deriving the mean $A(\text{Li})$. Particularly for clusters older than the Hyades, there is growing evidence that $A(\text{Li})$ above the Li-dip shows a more extensive range, especially toward lower $A(\text{Li})$, as a cluster ages (Deliyannis et al. 2018, in prep.). Equally concerning is the observational fact that the range in $A(\text{Li})$ for these samples, irrespective of the cluster $[\text{Fe}/\text{H}]$, exhibits a similar upper bound approaching $A(\text{Li}) = 3.35$. We will return to this point after discussing the trends in $A(\text{Li})$ among stars beyond the cluster turnoff.

5.4. Evolution on the Subgiant Branch and Beyond

The second empirical insight gained from the $A(\text{Li})$ measures comes from the color evolution illustrated in Fig. 7. There is a clear range of $A(\text{Li})$ between 2.75 and 3.35 for the stars at the turnoff with $B-V$ bluer than 0.5 but no statistical evidence for a variation with temperature/color or V . For stars with $B-V$ redder than 0.5, there is a clear decline in $A(\text{Li})$ as stars evolve across the

subgiant branch, reaching a typical abundance of $A(\text{Li}) \sim 1.25$ at the base of the red giant branch, near the expected location for the end of the FDU phase. The pattern of a distinct transition in $A(\text{Li})$ as a function of T_{eff} is reminiscent of the Li-dip on the blue/hotter side among less evolved main sequence stars. From the precision composite data for young clusters (Cummings et al. 2017), intermediate-age clusters (Anthony-Twarog et al. 2009; Cummings et al. 2012), and field stars (Ramírez et al. 2012), stars on the unevolved main sequence which were hotter than $T_{\text{eff}} \sim 6700$ K exhibit well-defined values of $A(\text{Li})$ between 3.2 and 3.4 or, at minimum, a range of $A(\text{Li})$ extending as high as these limiting values. For stars at $T_{\text{eff}} \sim 6600$ K and as old as or older than the Hyades, one can only find stars with minimal or undetectable $A(\text{Li})$, defining the approximate center of the Li-dip. This T_{eff} boundary is readily seen in intermediate-age and older clusters where the unevolved main sequence temperature pattern translates into a break at a specific V magnitude due to the evolution of the key mass range into an approximately vertical turnoff (see, e.g. Fig. 10 of Anthony-Twarog et al. (2009)).

If the physical mechanism defining the high mass boundary of the Li-dip is predominantly defined by the T_{eff} of the star, stars of higher mass which form with temperatures hotter than this limit might be expected to initiate Li-depletion upon crossing this boundary during post-main-sequence evolution toward and across the subgiant branch. For stars at the turnoff of NGC 2506, with $E(B - V) = 0.06$, the color boundary for $T_{\text{eff}} = 6700$ K should be $B - V = 0.43$. While the sample is small, the majority of stars between $B - V = 0.43$ and 0.5 do not show a dramatic drop in $A(\text{Li})$; the boundary of $B - V = 0.5$ is equivalent to $T_{\text{eff}} = 6450$ K, placing it already beyond the center of the Li-dip defined by lower mass stars. In short, dwarfs exhibit a distinct Li-dip while higher-mass subgiants in the same T_{eff} range do not. Since the Li-dip among dwarfs requires a few hundred million years to develop, the lack of a distinct boundary could arise from the more rapid evolutionary timescale for stars crossing the subgiant branch. This immediate lack of coupling by stars at the turnoff and the Li-dip temperature boundary is even more evident in the slightly older cluster, NGC 6819, where almost the entire turnoff region brighter than the Li-dip lies redward of the Li-dip T_{eff} boundary but these higher mass stars retain a range of $A(\text{Li})$ extending to 3.2 (Deliyannis et al. 2018, in prep.). Therefore, while T_{eff} can play a valuable role in marking the boundary for the initiation of extra mixing and/or Li dilution not predicted by SSET for stars on or leaving the main sequence, it supplies no particular insight into the physical mechanism

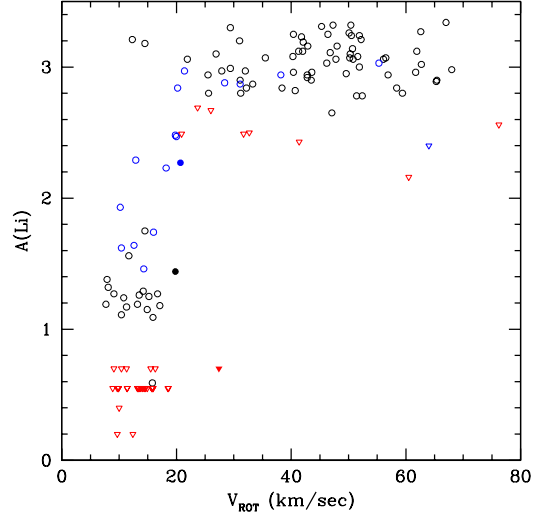


Figure 8. Li abundance as a function of rotational speed. Symbols have the same meaning as in Fig.5.

driving the process of depletion.

An alternative possibility emerges from the other significant stellar property which changes decisively for stars entering and crossing the subgiant branch, V_{rot} . Fig. 8 shows the trend of $A(\text{Li})$ as a function of V_{rot} for the stars used in Figures 5, 6, and 7. Symbols have the same meaning as in the previous figures. First, there is no apparent correlation between $A(\text{Li})$ and rotational speed. As discussed earlier, the majority of stars for which reliable $A(\text{Li})$ estimation was deemed implausible were rapid rotators ($V_{\text{rot}} > 30$ km s $^{-1}$). A significant concern for such rotators is that the increased blending of the neighboring lines makes it challenging to judge the continuum level and account for line contamination. Unlike dwarfs in the Hyades and Praesepe (Cummings et al. 2017), however, a metallicity less than half that of the younger clusters makes this less of an issue and clearly introduces no trend in the data for stars where $A(\text{Li})$ is detectable.

Second, keeping in mind that the $\sin i$ factor can move any star toward a lower than true rotation speed, i.e. to the left in Fig. 8, the sharp transition near $V_{\text{rot}} = 25$ km s $^{-1}$ is striking. Stars with $A(\text{Li})$ covering the range from 2.75 to 3.35 can have virtually any rotation speed from 12 to 65 km s $^{-1}$; by contrast, with only one exception, every star with $A(\text{Li})$ below 2.4 has V_{rot} below 25 km s $^{-1}$.

The significance of the distribution of $A(\text{Li})$ with V_{rot} among turnoff stars and giants becomes apparent when NGC 2506 is placed in the context of clusters ranging in age from 1.4 Gyr (NGC 7789) to NGC 3680 (1.7 Gyr) to NGC 6819 (2.25 Gyr). As detailed in Deliyannis et al. (2018, in prep.), for stars brighter than the Li-dip at the cluster turnoff, the range in V_{rot} extends above 100

km s^{-1} for the youngest cluster, declines to $\sim 60 \text{ km s}^{-1}$ for the intermediate-age cluster, and drops to $\sim 25 \text{ km s}^{-1}$ for the oldest. NGC 2506 therefore most resembles NGC 3680, taking into account the lower mass of the Li-dip at lower $[\text{Fe}/\text{H}]$. Equally relevant, as the cluster age rises, the fraction of stars at the turnoff and more massive than the Li-dip stars with depleted or undetectable Li rises from less than 15% to more than 70%. This trend also translates into a dramatic evolution of the Li among the giants. While more than half of the evolved stars in NGC 2506 have detectable Li, only 7 of the 51 stars classed as subgiants or giants in NGC 6819 have detectable Li (Deliyannis et al. 2018, in prep.).

Before continuing with the distribution of $A(\text{Li})$ among the giants on the FRG branch, we can ask how well the empirical observations of Li evolution from the main sequence through the subgiant branch agree with the predictions of standard stellar evolution theory, in the absence of two critically important processes, rotation-induced mixing and thermohaline mixing. The general answer is that, on many details, they don't agree. As first emphasized by Pasquini et al. (2004) using the models of Charbonnel & Talon (1999); Palacios et al. (2003) applied to the sparse data for IC 4651, models without rotation are incapable of explaining any decline in $A(\text{Li})$ among intermediate mass stars ($M = 1.8 M_{\odot}$) on the main sequence and beyond until the FDU, well across the Hertzsprung gap, in contradiction with the cluster data. By contrast, stellar models with the same mass but rotating above 100 km s^{-1} show significant depletions in atmospheric Li initiated at temperatures much hotter than in the non-rotating stars and comparable to the T_{eff} of stars just leaving the main sequence.

The analysis of IC 4651 was revised using the newer models of Charbonnel & Lagarde (2010) to include rotation-induced mixing, internal gravity waves, atomic diffusion, and thermohaline mixing and expanded to include the evolutionary pattern for Be, once again confirming the need for additional mixing processes beyond simple convection to explain the abundance patterns observed in field stars and clusters (Smiljanic et al. 2010). With the exceptionally well-defined trend of $A(\text{Li})$ across the subgiant branch of NGC 2506, we can more effectively test the model predictions using the discussion of Charbonnel & Lagarde (2010). The closest model analog to the stars at the turnoff and along the giant branch of NGC 2506 which have all three variants: standard evolution, standard with thermohaline mixing, and standard with thermohaline mixing and rotation are the $1.5 M_{\odot}$ models with rotation speeds near 0 or 110 km s^{-1} . Note that the model metallicity is solar and the rotation speed is larger than observed for the stars in NGC 2506, but our primary interest is in the

qualitative pattern.

If we use standard evolution with or without thermohaline mixing, non-rotating stars leaving the main sequence retain their primordial $A(\text{Li})$ until they are almost 1600 K cooler than the turnoff T_{eff} , or $(B - V) = 0.75$ for NGC 2506. At the hottest point of the turnoff, the surface convection zone (SCZ) occupies a tiny fraction by mass of the outermost layers. As the model evolves to cooler T_{eff} along the subgiant branch, the SCZ deepens substantially and continuously. In standard theory (e.g. Deliyannis, Demarque, & Kawaler (1990)), the Li abundance as a function of depth has not been altered substantially while on the the main sequence until a depth is reached where Li is broken apart by energetic protons, the Li preservation boundary. Below that boundary, Li declines steeply with depth. Therefore, the surface Li abundance stays constant until the SCZ deepens sufficiently to reach the Li preservation boundary. As noted earlier, this happens at $T_{\text{eff}} \sim 5600 \text{ K}$. Further evolution begins to reveal the impact of the first dredge-up, as the SCZ deepens into regions where Li was destroyed during the MS and pre-MS phases and are thus now devoid of Li. Even as the SCZ deepens, the model expands and these layers are now much cooler than they were during the MS: no further Li destruction occurs at the base of the SCZ. Instead, convection mixes the outermost regions that still contain Li with those regions that are devoid of Li, resulting in a decrease of the surface Li abundance, i.e., subgiant dilution.

This decrease is a steep function of decreasing T_{eff} because by the time the SCZ reaches the base of the FRG branch, it includes more than half of the stellar mass. By contrast, the Li preservation region occupies only a small fraction of the stellar mass, so the total dilution of surface Li is roughly 1.8 dex (Deliyannis, Demarque, & Kawaler 1990; Charbonnel & Lagarde 2010). The SCZ reaches a maximum depth near the base of the FRG branch at $\sim 4800 \text{ K}$, after which the base of the SCZ recedes slowly toward the surface, as the model evolves up the FRG branch. Standard theory predicts no further depletion of surface Li up the giant branch, thereby establishing the *subgiant diluted Li plateau*, namely a constant Li abundance up the FRG. If the turnoff $A(\text{Li}) \sim 3.3$, then the diluted plateau is predicted to have $A(\text{Li}) \sim 1.5$. If $A(\text{Li})$ of the star leaving the turnoff is lower, either due to a lower primordial Li value associated with a lower metallicity cluster and/or due to non-standard Li depletion on the main sequence, then the diluted plateau $A(\text{Li})$ could easily approach $A(\text{Li}) = 1.2$. This would be consistent with the plateau of Li abundances seen in Figure 6 and 7. But what about those stars with $A(\text{Li})$ lying substantially below the diluted Li plateau?

Subgiant evolution can show the effects of non-standard surface Li depletion mechanisms that might

have acted during the MS and beyond, and that might have reduced the amount of Li in the Li preservation region. In the case of the models of Charbonnel & Lagarde (2010), inclusion of rotation and rotationally-induced mixing produces an immediate and continuous decline in $A(\text{Li})$ as soon as the star begins evolving away from the main sequence toward the giant branch. By the end of the first dredge-up phase the atmospheric $A(\text{Li})$ is reduced to less than 0.5. It is expected that adoption of a lower initial rotation rate would generate the same trend, but approach a higher limit for $A(\text{Li})$ beyond the first dredge-up. Exactly how the final value for $A(\text{Li})$ correlates with increased V_{rot} requires extensive modelling beyond those currently available.

Moving beyond the base of the FRG branch, the deficiency in Li among the clump stars is predictable since all these stars have supposedly undergone He-flash, generating mixing which could reduce and/or eliminate any remaining signs of the element in their atmospheres as they arrive at the red giant tip. While burning He in a stable configuration on the clump, the $A(\text{Li})$ should remain unchanged until the star begins its ascent up the asymptotic giant branch and approaches the second dredge-up phase.

A more uncertain interpretation applies to the concentration of Li-deficient stars at the base of the giant branch. The key structural feature which kicks in near this phase of evolution is the FDU. As already noted, if the surface convection zone reaches deep enough, it can mix atmospheric Li with Li-depleted layers well below the Li-preservation zone, potentially causing a sudden and significant decrease in the observed $A(\text{Li})$, as seen in Fig. 5 near $V = 14.8$. If this is the case, why then do the majority of stars on the FRG branch between $V = 14.6$ and 13 in Fig. 5 have measurable and *constant* $A(\text{Li})$?

One potential solution is that the difference between measurable and detectable Li among the spectra is small enough that only a slight change in the strength of the line will shift a star from one category to the other, i.e. the bimodal Li distribution among these giants is an artifact of the spectra. To illustrate why this fails, we show in Fig. 9 a comparison of two stars at the base of the giant branch with virtually identical colors and magnitudes, star 1301 with $A(\text{Li})$ near 1.56 and star 7008 with only an upper limit near $A(\text{Li}) = 0.6$. It is clear that there is a distinct difference in the strength of the Li line for these two stars, consistent with their classification, even though all other lines have the same strength within the spectroscopic uncertainties.

Assuming that the majority of these stars are members and do not represent a low-luminosity extension of the red giant clump, two plausible options exist: (a) these stars aren't single stars, but instead are evolved bi-

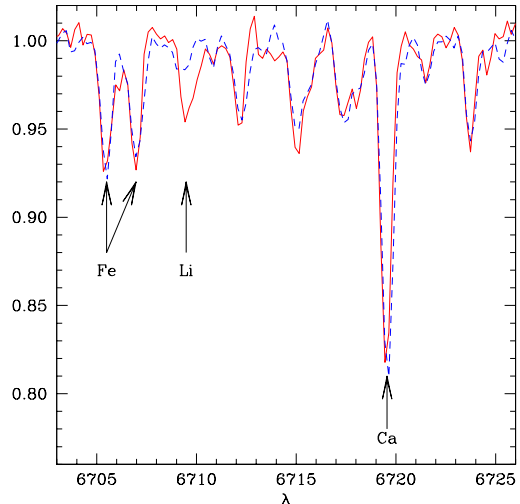


Figure 9. Closeup of Lithium line region in two stars at the base of the giant branch. The red spectrum traces star 1301, the blue spectrum star 7008. A number of lines in the Li region are identified.

aries/blue stragglers approaching the base of the giant branch at a higher luminosity, or (b) the stars with more extreme Li-depletion than the Li-plateau stars are those which initially had the highest rotation speeds and have been systematically more affected by the mixing processes controlled by rotation and stellar spindown. We reiterate that one of the stars among this group has a spectroscopic $[\text{Fe}/\text{H}]$ near solar indicating that, despite the radial velocity agreement with the cluster value, it may be a field interloper.

From Fig. 7, among the stars with measurable Li, there is little evidence for a decline in $A(\text{Li})$ as one moves up the giant branch to the level of the clump. Instead, from 16 FRGs (open circles in Figs. 5, 6, and 7), the stars have $A(\text{Li}) = 1.25$ with a scatter of ± 0.11 dex. If one star near the base of the FRG is excluded, the average becomes 1.22 ± 0.08 , only slightly higher than expected from the precision of the measures, but significantly lower than found among the stars at the turnoff. For SSET and for models with rotational mixing on the main sequence, $A(\text{Li})$ for a star is predicted to remain constant at the value it has attained after completion of the FDU.

The next key change predicted in the surface $A(\text{Li})$ occurs once the stars pass beyond the red giant bump. The red giant bump represents an evolutionary slowdown and reversal as the hydrogen-burning shell passes across the chemical composition discontinuity created by the high-water mark of the convection zone as the stars evolved toward and up the giant branch. The change in molecular weight and H concentration allows the giant to support itself at a lower luminosity and then evolve back up the giant branch at a slower rate, causing a den-

sity excess in the distribution of giants. Standard models predict that stars evolving beyond the bump will experience no change in $A(\text{Li})$ until they reach the tip of the giant branch. By contrast, if one includes thermohaline mixing, stars brighter than the bump will decrease their lithium by 0.4 dex. The location of the red giant bump in NGC 2506, predicted by VR isochrones with age between 1.8 and 1.9 Gyr and $[\text{Fe}/\text{H}] = -0.29$, is between $V = 12.95$ and 12.7 , above the observed level of the clump. Clearly, there is no excess concentration of stars in this magnitude range in Fig. 5. However, the [Charbonnel & Lagarde \(2010\)](#) models for the $1.5 M_{\odot}$ with rotation ($V_{\text{rot}} = 110 \text{ km s}^{-1}$) demonstrate that the presence of rotation will shift the location of the red giant bump and the start of thermohaline mixing to a lower luminosity on the giant branch, typically 40% fainter for the bump and a factor of almost 8 for the mixing trigger, placing the mixing phase only 3-4 times brighter than the red giant bump. While the size of the change will depend upon the specific size of the rotation, inclusion of rotation should move the bump fainter than the level of the red giant clump. Equally important, additional depletion of Li caused by thermohaline mixing should begin to show among stars on the FRG branch no more than a magnitude brighter than the clump. Thus, the redefinition of the FRG branch passing through star 2402 with detectable Li just below $A(\text{Li}) = 0.6$ is consistent with a significant decline from $A(\text{Li}) = 1.25$ caused by mixing in a star beyond the red giant bump. The other stars brighter than 2402 at comparable colors would then be either binaries undergoing peculiar evolution or stars ascending the asymptotic giant branch.

6. SUMMARY AND CONCLUSIONS

HYDRA spectroscopy of 287 stars in the field of NGC 2506 has been used in conjunction with published proper-motion membership and position in the CMD to identify highly probable, single-star members of the cluster for further analysis. The survey included 24 stars within the previously studied area of the cluster and 135 stars outside the cluster area for which the only available information was the location in the CMD. Of these 159, 94 proved to be probable radial-velocity members, adding a critical number of stars to evolutionary phases of the CMD which are normally poorly, if at all, populated. Abundance analysis for metallicity determination, dominated by the richer and stronger line profiles of the cooler stars, confirms that NGC 2506 is moderately metal-poor, with $[\text{Fe}/\text{H}]$ near -0.3.

Returning to the primary focus of the investigation, the evolution of Li within the cluster as a function of mass, a number of conclusions stand out:

There is an intrinsic spread in $A(\text{Li})$ among the stars at the vertical turnoff, though the range is independent

of stellar luminosity or color. Since all the observed turnoff stars lie brighter than the Li-dip and, by SSET, have retained their initial Li abundance unchanged by evolution, the mean $A(\text{Li})$ for the cluster is calculated to be 3.05 ± 0.16 , consistent with a lower initial abundance than the sun ([Asplund et al. 2009](#)), as predicted for cluster which is a factor of two below solar in $[\text{Fe}/\text{H}]$. It is noted, however, that the full range of the sample in $A(\text{Li})$ extends from 2.75 to 3.35, comparable to that found among stars blueward of the Li-dip in clusters of solar metallicity or higher.

Upon exiting the turnoff region and evolving across the subgiant branch, the stars undergo a well-delineated decline in atmospheric Li, declining from a mean of $A(\text{Li}) = 3.05$ to a plateau value of 1.25 by the base of the FRG branch. While it has been obvious for decades that the typical red giant contains less Li than expected for a star of the same mass on the main sequence, it has been a challenge to identify precisely when and where the depletion occurs. Stars fainter than the clump in clusters of intermediate age exhibit depleted Li, but the degree of depletion can vary by a factor of ten and it can be difficult to assess if the star is truly a first-ascent or red clump giant.

We reiterate that the evolutionary phase under discussion is not the vertical turnoff region. Intermediate-age clusters like NGC 3680 and NGC 752 do show a spread in $A(\text{Li})$ ranging from 3.3 to 2.6 at the top of the vertical turnoff ([Anthony-Twarog et al. 2009](#)), virtually identical to the range found in NGC 2506. IC 4651 exhibits the same pattern, but is the one cluster in the 1-2 Gyr age category to include multiple stars populating the subgiant branch between the vertical turnoff and the red giant branch. [Pasquini et al. \(2004\)](#) have studied a limited sample of stars in IC 4651 and find four at the top of the turnoff and one at a temperature intermediate between the turnoff stars and the red clump which have $A(\text{Li})$ between 2.4 and 1.6. Note that the one star with a T_{eff} placing it in the subgiant region has $A(\text{Li}) = 2.1$. For the first time, the mapping of a subgiant branch using stars outside the Li-dip demonstrates that these stars continuously deplete Li as they evolve to the base of the FRG branch, irrespective of whatever mechanism, if any, produces the dispersion among stars at the top of the turnoff.

A contributing factor leading to the onset Li-depletion on the subgiant branch appears to be the spindown of the stars as they evolve to cooler temperatures at almost constant luminosity. Stars at the vertical turnoff within the $A(\text{Li})$ range discussed earlier can have any rotation speed between $\sim 10 \text{ km s}^{-1}$ and 70 km s^{-1} , with the caveat that the true rotation speed could be higher and that the spectra have resolution which limits the V_{rot} to a minimum approaching 10 km s^{-1} . There is

no correlation between luminosity and/or temperature and V_{rot} . By contrast, as stars evolve across the subgiant branch and the typical V_{rot} declines from a minimum of 25 km s^{-1} to an average near 13 km s^{-1} , $A(\text{Li})$ drops steadily to 1.25. This pattern fits perfectly within the trend defined by NGC 7789, NGC 3680, and NGC 6819, where the fraction of turnoff and giant stars with detectable Li is strongly correlated with the spread in rotation speed among stars hotter than the Li-dip; the larger the range in speed at a given age, the more likely the turnoff stars will have a modest range in $A(\text{Li})$ with a mean at or above 3.0, and the more likely that the giants will exhibit detectable Li near 1 (Deliyannis et al. 2018, in prep.).

It should be noted that the V_{rot} distribution for stars brighter than the Li-dip at the turnoff and on the giant branch of IC 4651 (Meibom, Andersen, & Nordström 2002) is virtually identical to that in NGC 3680. For stars at the turnoff, the range is from $\sim 10 \text{ km s}^{-1}$ to more than 60 km s^{-1} while the giants exhibit a small scatter near 1 km s^{-1} (Meibom, Andersen, & Nordström 2002). The uncertainty in the latter velocity measures is analogous to that for Carlberg (2014) rather than our HYDRA data. Unfortunately, when binaries are eliminated, the current number of stars with reliable Li determinations brighter than the Li-dip is too small to shed any statistical light on the question. A comprehensive survey of this cluster with a significant expansion of the spectroscopic sample could prove invaluable.

The Li pattern exhibited at the turnoff is consistent with the predictions of stellar models of low/intermediate mass which include rotation-induced mixing on the main sequence and beyond (Charbonnel & Lagarde 2010). The growing dispersion in Li for stars on the blue side of the Li-dip as clusters age from 1 to 2 Gyrs then becomes a reflection of the initial spread in V_{rot} acting over time to reduce the absolute Li at Hyades age from a uniform value at or above $A(\text{Li}) = 3.0$. This dispersion is then coupled with the significant spindown of all the stars evolving along the subgiant branch, reducing the Li abundance to a typical value of 1.2 by the base of the FRG and the end of the first dredge-up. If the decline in $A(\text{Li})$ at the start of the subgiant branch is not tied to the evolution of the rotation rate but simply defines the start of the first dredge-up, this phase is triggered at a much higher T_{eff} (6450 K) than predicted by the non-rotating models (5600 K).

A fundamental challenge to this qualitative explanation for the spread in $A(\text{Li})$ among the turnoff stars is presented by the absence of a comparable spread among the evolved stars of the FRG branch. The dispersion in $A(\text{Li})$ for stars at the turnoff is twice that among the giants; if stars leave the main sequence with a factor of 4 range in the Li abundance due to the range in

V_{rot} , why doesn't that spread persist among stars on the FRG branch? An alternative solution to the dispersion question is presented by diffusion among the metal-deficient stars at the cluster turnoff. For very thin SCZs among stars in the T_{eff} range 6800 K to 7100 K, Li can undergo radiative acceleration into the SCZ, creating potentially significant surface overabundances, if the radiative acceleration region is much larger by mass fraction than the SCZ (Richer & Michaud 1993). If the initial $A(\text{Li})$ for the metal-poor NGC 2506 was ~ 3.0 , this mechanism could create surface $A(\text{Li})$ as high as 3.3 or higher, without destroying Li inside the star. Inside the star, below the radiative acceleration boundary, Li sinks, with a small amount of it potentially reaching depths where some, but not much, might be destroyed. For stars cooler than about 6700 K, the radiative acceleration boundary is within the SCZ, so only downward diffusion at the base of the SCZ can occur. The net result is that as stars leave the main sequence and the SCZ grows, mixing of the inhomogeneous layers returns $A(\text{Li})$ to the initial value of ~ 3.0 with only a modest dispersion. Beyond that point, whatever mechanisms exist to deplete Li on the subgiant branch and beyond act on a significantly more homogeneous initial abundance. Clearly, deciding on the relative viability of either process is beyond the scope of the current observations.

Moving to the FRG branch, it is tempting to associate the handful of Li-deficient giants at the base of the FRG with the FDU as the SCZ accesses deeper and hotter layers below the atmosphere. If the first dredge-up is being outlined by the stars with upper limits to Li, it would be beneficial to look for other signatures of mixed processed nuclear material, e.g. $^{12}\text{C}/^{13}\text{C}$ ratios, in the atmospheres of these and the more evolved stars (e.g., Charbonnel & Lagarde 2010; Karakas & Lattanzio 2014). To date, $^{12}\text{C}/^{13}\text{C}$ ratios have been measured for 3 giants by Mikolaitis et al. (2011) and 3 single-star (3265 excluded) giants by Carlberg, Cunha, & Smith (2016). Five of the 6 stars are located in the clump and one sits 1.5 mag above the clump, classified as a red-giant-tip star by Mikolaitis et al. (2011), though this becomes debatable in light of the CMD position of 2402. Ignoring for now the one star with a lower limit to the $^{12}\text{C}/^{13}\text{C}$ ratio of 10, the remaining 5 stars have an average ratio of 10 ± 2 , indicating that the stars all have the same $^{12}\text{C}/^{13}\text{C}$ ratio, within the uncertainties for the individual measures. This low value is also consistent with rotating models which include thermohaline mixing, whether the star is at the red giant tip or completing the second dredge-up phase (Charbonnel & Lagarde 2010). The models do predict a significantly higher value above 20 for stars completing the first dredge-up. So, while the $^{12}\text{C}/^{13}\text{C}$ ratio can't distinguish between a first or second-ascent red giant, it should provide insight

into the status of the Li-depleted giants at the base of the FRG.

For stars with detectable Li on the FRG, within the scatter, there appears to be no evidence for a systematic depletion of Li up to the level of the red clump. The one star (2402) above the clump with detectable Li, if it defines the path of the FRG above the clump, exhibits depletion relative to the other giants which is consistent with a post-bump giant undergoing thermohaline mixing. The stars within the clump, with one anomalously blue exception, exhibit only upper limits below the level of star 2402. For comparison, with four measured clump stars at higher resolution, [Carlberg, Cunha, & Smith \(2016\)](#) determine a detectable LTE Li abundance (the appropriate comparison for our data) for two stars and an upper limit for two more. The average of the two stars with measured Li is $A(\text{Li}) = 0.63$ from individual values with $\sigma_{\text{Li}} = 0.14$. The two stars with only upper limits have average limits of $A(\text{Li}) = 0.45$. These esti-

mates are clearly below 1.25 and totally consistent with our clump determinations obtained at lower resolution.

The authors are indebted to the referee for a thorough and invaluable reading of the original manuscript, identifying a number of potential points of confusion and a significant error in one of our equations. The paper has definitely been improved as a result. The authors gratefully acknowledge extensive use of the WEBDA⁵ database, maintained at the University of Brno by E. Paunzen, C. Stutz and J. Janik. We also express appreciation to Jeffrey Cummings for sharing spectroscopic data with us. Support was provided to BJAT, DLB and BAT through NSF grant AST-1211621 and to CPD through AST-1211699.

Facility: WIYN:3.5m

Software: IRAF

REFERENCES

- Ahn, C. P., Alexandroff, R., Allende Prieto, C., et al. 2014, *ApJS*, 211, 17
- Allende Prieto, C., Rebolo, R., García López, R. J., et al. 2000, *AJ*, 120, 1516
- Anthony-Twarog, B. J., Atwell, J., & Twarog, B. A. 2005, *AJ*, 129, 872
- Anthony-Twarog, B. J., Deliyannis, C. P., Twarog, B. A., Croxall, K. V., & Cummings, J. 2009, *AJ*, 138, 1171
- Anthony-Twarog, B. J., Deliyannis, C. P., & Twarog, B. A. 2016, *AJ*, 152, 192 (AT16)
- Anthony-Twarog, B. J., & Twarog, B. A. 2000, *AJ*, 119, 2282
- Arbib, M. A. 2002, *The Handbook of Brain Theory and Neural Networks*, 2nd edn. (Cambridge, MA: MIT Press)
- Arentoft, T., De Ridder, J., Grundahl, F., et al. 2007, *A&A*, 465, 965
- Asplund, M., Grevasse, N., Sauval, A. J., & Scott, P. 2009, *ARA&A*, 47, 481
- Bailer-Jones, C. A. L., Irwin, M., Gilmore, G., & von Hippel, T. 1997, *MNRAS*, 292, 157
- Balachandran, S. 1995, *ApJ*, 446, 203
- Balachandran, S., Anthony-Twarog, B. J., & Twarog, B. A. 1991, *The Formation and Evolution of Star Clusters*, ed K. Janes (ASP Conf. Ser. 13; San Francisco: ASP), 544
- Balachandran, S. C., Mallik, S., & Lambert, D. L. 2010, *MNRAS*, 410, 2526
- Bruntt, H., Basu, S., Smalley, B., et al. 2012, *MNRAS*, 423, 122
- Carlberg, J. K. 2014, *AJ*, 147, 138
- Carlberg, J. K., Cunha, K., & Smith, V. V. 2016, *ApJ*, 827, 129
- Carretta, E., Bragaglia, A., Gratton, R. G., & Tosi, M. 2004, *A&A*, 422, 951
- Casey, A. R., Ruchti, G., Masseron, T., et al. 2016, *MNRAS*, 461, 3336
- Charbonnel, C., & Lagarde, N. 2010, *A&A*, 522, 10
- Charbonnel, C., & Talon, S. 1999, *A&A*, 351, 635
- Chen, Y. Q., Nissen, P. E., Benoni, T., & Zhao, G. 2001, *A&A*, 371, 943
- Chiu, L.-T. G., & van Altena, W. F. 1981, *ApJ*, 243, 827
- Coc, A., Uzan, J.-P., & Vangioni, E. 2014, *JCAP*, 10, 50
- Cortés, C., Silva, J. R. P., Recio-Blanco, A., et al. 2009, *ApJ*, 704, 750
- Cummings, J. D. 2008, PhD Thesis, University of Indiana
- Cummings, J. D., Deliyannis, C. P., Anthony-Twarog, B. J., Twarog, B. A., & Maderak, R. M. 2012, *AJ*, 144, 137
- Cummings, J. D., Deliyannis, C. P., Maderak, R. M., & Steinhauer, A. 2017, *AJ*, 153, 128
- Dafonte, C., Fustes, D., Manteiga, M. et al. 2016, *A&A*, 594, A68
- Deliyannis, C. P., Anthony-Twarog, B. J., Lee-Brown, D. B., & Twarog, B. A. 2018, in preparation
- Deliyannis, C. P., Demarque, P., & Kawaler, S. D. 1990, *ApJS*, 73, 21
- Deliyannis, C. P., & Pinsonneault, M. H. 1993, *IAU Colloquium 137, Inside the Stars*, ed. W. W. Weiss & A. Baglin (ASP Conf. Ser. 40; San Francisco: ASP), 174
- Deliyannis, C. P., Pinsonneault, M. H., & Duncan, D. K. 1993, *ApJ*, 414, 740
- Deliyannis, C. P., Steinhauer, A., & Jeffries, R. D. 2002, *ApJ*, 577, L39
- Dobrovolskas, V., Kučinskas, A., Bonifacio, P. et al. 2014, *A&A*, 565, 121
- Edvardsson, B., Andersen, J., Gustafsson, B., et al. 1993, *A&A*, 275, 101
- Francois, P., Pasquini, L., Biazzo, K., Bonifacio, P., & Palsa, R. 2013, *A&A*, 552, 136
- Friel, E. D., & Janes, K. A. 1993, *A&A*, 267, 75
- Friel, E. D., Janes, K. A., Tavares, M., et al. 2002, *AJ*, 124, 2693
- Fu, X., Romano, D., Bragaglia, A., et al. 2017, arXiv:1711.04829
- Gray, R. O., & Corbally, C. J. 1994, *AJ*, 107, 742
- Gruyters, P., Lind, K., Richard, O., et al. 2016, *A&A*, 589, 61
- Gruyters, P., Nordlander, T., & Korn, A. J. 2014, *A&A*, 567, 72
- Hill, V., & Pasquini, L. 2000, *IAU Symp. 198, The Light Elements and Their Evolution*, ed. L. da Silva, R. de Medeiros, & M. Spite (San Francisco: ASP), 293
- Jacobson, H. R., Friel, E. D., & Pilachowski, C. A. 2011, *AJ*, 141, 58
- Jones, B. F., Fischer, D., Shetrone, M., & Soderblom, D. R. 1997, *AJ*, 114, 352

⁵ <http://webda.physics.muni.cz>

- Karakas, A. I., & Lattanzio, J. C. 2014, *PASA*, 31, 30
- Kim, S.-L., Chun, M.-Y., Park, B.-G., et al. 2001, *AcA*, 51, 49
- Kumar, Y. B., Reddy, B. E., & Lambert, D. L. 2011, *ApJL*, 730, 12
- Kupka, F., Piskunov, N., Ryabchikova, T. A., Stempels, H. C., & Weiss, W. W. 1999, *A&AS*, 138, 119
- Kurucz, R. L. 1992, *IAU Symp. 149, The Stellar Populations of Galaxies*, ed. B. Barbuy & A. Renzini (Dordrecht: Kluwer), 225
- Landolt, A. U. 1992, *AJ*, 104, 340
- Lee, S. H., Kang, Y.-W., & Ann, H. B. 2012, *MNRAS*, 425, 1567
- Lee, S. H., Kang, Y.-W., & Ann, H. B. 2013, *MNRAS*, 432, 1672
- Lee-Brown, D. B., Anthony-Twarog, B. J., Deliyannis, C. P., Rich, E., & Twarog, B. A. 2015, *AJ*, 149, 121
- Li, X.-R., Pan, R.-Y., & Duan, F.-Q. 2017, *Research in Astronomy & Astrophysics*, 17, 36
- Lind, K., Primas, F., Charbonnel, C., Grundahl, F., & Asplund, M. 2009, *A&A*, 503, 545
- Lucatello, S., & Gratton, R. G. 2003, *A&A*, 406, 691
- Maderak, R. M., Deliyannis, C. P., King, J. R., & Cummings, J. D. 2013, *AJ*, 146, 143
- Manteiga, M., Ordóñez, D., Dafonte, C., & Arcay, B. 2010, *PASP*, 122, 608
- Marconi, G., Hamilton, D., Tosi, M., & Bragaglia, A. 1997, *MNRAS*, 291, 763
- McClure, R. D., Twarog, B. A., & Forrester, W. T. 1981, *ApJ*, 243, 841
- Meibom, S., Andersen, J., & Nordström, B. 2002, *A&A*, 386, 187
- Mermilliod, J.-C., & Mayor, M. 2007, *A&A*, 470, 919
- Mermilliod, J.-C., Mayor, M., & Udry, S. 2008, *A&A*, 485, 303
- Mikolaitis, S., Tautvaišienė, G., Gratton, R., Bragaglia, A., & Carretta, E. 2011, *MNRAS*, 416, 1092
- Minniti, D. 1995, *A&AS*, 113, 299
- Monaco, L., Boffin, H. M. J., Bonifacio, P., et al. 2014, *A&A*, 564, L6
- Netopil, M., Paunzen, E., Heiter U., & Soubiran, C. 2016, *A&A*, 585, 150
- Palmerini, S., Cristallo, S., & Busso, M., et al. 2011, *ApJ*, 741, 26
- Palacios, A., Talon, S., Charbonnel, C., & Forestini, M. 2003, *A&A*, 399, 603
- Pasquini, L., Randich, S., Zoccali, M., et al. 2004, *A&A*, 424, 951
- Pinsonneault, M. 1997, *ARA&A*, 35, 557
- Ramírez, I., Allende Prieto, C. & Lambert, D. L. 2013, *ApJ*, 764, 78
- Ramírez, I., Fish, J. R., Lambert, D. L., & Allende Prieto, C. 2012, *ApJ*, 756, 46
- Ramírez, I., & Meléndez, J. 2005, *ApJ*, 626, 465
- Reddy, A. B. S., Giridhar, S., & Lambert, D. L. 2012, *MNRAS*, 419, 1350
- Richer, J. & Michaud, G. 1993, *ApJ*, 416, 312
- Snedden, C. 1973, *ApJ*, 184, 839
- Snider, D., Allende Prieto, C., von Hippel, T., et al. 2001, *ApJ*, 562, 528
- Randich, S., Pace, G., Pastori, L., & Bragaglia, A. 2009, *A&A*, 496, 441
- Santos, N. C., Lovis, C., Pace, G., Meléndez, J., & Naef, D. 2009, *A&A*, 493, 309
- Silva Aguirre, V., Ruchti, G. R., Hekker, S., et al. 2014, *ApJL*, 784, 16
- Smiljanic, R., Pasquini, L., Charbonnel, C., & Lagarde, N. 2010, *A&A*, 510, 50
- Steinhauer, A. 2003, PhD thesis, Indiana University
- Steinhauer, A., & Deliyannis, C. P. 2004, *ApJ*, 614, L65
- Stetson, P. B. 1987, *PASP*, 99, 191
- Takeda, Y., & Tajitsu, A. 2017, *PASJ*, 69, 74
- Twarog, B. A., Ashman, K., & Anthony-Twarog, B. J. 1997, *AJ*, 114, 2556
- Twarog, B. A., Anthony-Twarog, B. J., Deliyannis, C. P., & Thomas, D. T. 2015, *AJ*, 150, 134
- Waters, C. Z., & Hollek, J. K. 2013, *PASP*, 125, 1164
- VandenBerg, D. A., Bergbusch, P. A., & Dowler, P. D. 2006, *ApJS*, 162, 375
- Van Stockum, P., Matson, R., Deliyannis, C., Sarajedini, A., & Platais, I. 2005, *BAAS*, 37, 71.06 (VS)